



HAL
open science

Metallicity Distribution Function of the Eridanus II Ultra-faint Dwarf Galaxy from Hubble Space Telescope Narrowband Imaging

Sal Wanying Fu, Daniel Weisz, Else Starckenburg, Nicolas Martin, Alexander Ji, Ekta Patel, Michael Boylan-Kolchin, Patrick Côté, Andrew Dolphin, Nicolas Longeard, et al.

► **To cite this version:**

Sal Wanying Fu, Daniel Weisz, Else Starckenburg, Nicolas Martin, Alexander Ji, et al.. Metallicity Distribution Function of the Eridanus II Ultra-faint Dwarf Galaxy from Hubble Space Telescope Narrowband Imaging. *The Astrophysical Journal*, 2022, 925 (1), pp.6. 10.3847/1538-4357/ac3665 . hal-03585520

HAL Id: hal-03585520

<https://hal.science/hal-03585520v1>

Submitted on 24 Feb 2022

HAL is a multi-disciplinary open access archive for the deposit and dissemination of scientific research documents, whether they are published or not. The documents may come from teaching and research institutions in France or abroad, or from public or private research centers.

L'archive ouverte pluridisciplinaire **HAL**, est destinée au dépôt et à la diffusion de documents scientifiques de niveau recherche, publiés ou non, émanant des établissements d'enseignement et de recherche français ou étrangers, des laboratoires publics ou privés.



Distributed under a Creative Commons Attribution 4.0 International License



Metallicity Distribution Function of the Eridanus II Ultra-faint Dwarf Galaxy from Hubble Space Telescope Narrowband Imaging

Sal Wanying Fu¹ , Daniel R. Weisz¹ , Else Starkenburg², Nicolas Martin³ , Alexander P. Ji^{4,5} , Ekta Patel^{1,6} , Michael Boylan-Kolchin⁷ , Patrick Côté⁸ , Andrew E. Dolphin^{9,10} , Nicolas Longeard¹¹, Mario L. Mateo¹², and Nathan R. Sandford¹

¹ Department of Astronomy, University of California, Berkeley, Berkeley, CA 94720, USA; swfu@berkeley.edu

² Kapteyn Astronomical Institute, University of Groningen, Postbus 800, 9700 AV, Groningen, the Netherlands

³ Université de Strasbourg, Observatoire astronomique de Strasbourg, UMR 7550, F-67000 Strasbourg, France

⁴ Department of Astronomy & Astrophysics, University of Chicago, 5640 South Ellis Avenue, Chicago, IL 60637, USA

⁵ Kavli Institute for Cosmological Physics, University of Chicago, Chicago, IL 60637, USA

⁶ Miller Institute for Basic Research in Science, 468 Donner Lab, Berkeley, CA 94720, USA

⁷ Department of Astronomy, The University of Texas at Austin, 2515 Speedway, Stop C1400, Austin, TX 78712-1205, USA

⁸ National Research Council of Canada, Herzberg Astronomy and Astrophysics Research Centre, Victoria, BC V9E 2E7, Canada

⁹ Raytheon Technologies, 1151 East Hermans Road, Tucson, AZ 85756, USA

¹⁰ Steward Observatory, University of Arizona, 933 North Cherry Avenue, Tucson, AZ 85721-0065 USA

¹¹ Laboratoire d'astrophysique, École Polytechnique Fédérale de Lausanne (EPFL), Observatoire, 1290 Versoix, Switzerland

¹² Department of Astronomy, University of Michigan, 311 West Hall, 1085 South University Avenue, Ann Arbor, MI 48109, USA

Received 2021 August 20; revised 2021 October 29; accepted 2021 November 2; published 2022 January 20

Abstract

We use deep narrowband CaHK (F395N) imaging taken with the Hubble Space Telescope (HST) to construct the metallicity distribution function (MDF) of Local Group ultra-faint dwarf galaxy Eridanus II (Eri II). When combined with archival F475W and F814W data, we measure metallicities for 60 resolved red giant branch stars as faint as $m_{F475W} \sim 24$ mag, a factor of $\sim 4\times$ more stars than current spectroscopic MDF determinations. We find that Eri II has a mean metallicity of $[\text{Fe}/\text{H}] = -2.50^{+0.07}_{-0.07}$ and a dispersion of $\sigma_{[\text{Fe}/\text{H}]} = 0.42^{+0.06}_{-0.06}$, which are consistent with spectroscopic MDFs, though more precisely constrained owing to a larger sample. We identify a handful of extremely metal-poor star candidates (EMP; $[\text{Fe}/\text{H}] < -3$) that are marginally bright enough for spectroscopic follow-up. The MDF of Eri II appears well described by a leaky box chemical evolution model. We also compute an updated orbital history for Eri II using Gaia eDR3 proper motions, and find that it is likely on first infall into the Milky Way. Our findings suggest that Eri II underwent an evolutionary history similar to that of an isolated galaxy. Compared to MDFs for select cosmological simulations of similar mass galaxies, we find that Eri II has a lower fraction of stars with $[\text{Fe}/\text{H}] < -3$, though such comparisons should currently be treated with caution due to a paucity of simulations, selection effects, and known limitations of CaHK for EMPs. This study demonstrates the power of deep HST CaHK imaging for measuring the MDFs of UFDs.

Unified Astronomy Thesaurus concepts: Dwarf galaxies (416); HST photometry (756); Stellar abundances (1577)

1. Introduction

The advent of wide-field photometric surveys at the turn of the 21st century has accelerated the discovery of ultra-faint dwarf galaxies (UFDs; e.g., Willman et al. 2005; Belokurov et al. 2007; Bechtol et al. 2015; Koposov et al. 2015; Laevens et al. 2015) around the Milky Way (MW). These galaxies currently make up the faintest end of the galaxy luminosity function, defined tentatively by Simon (2019) as being fainter than $10^5 L_{\odot}$. There are strong cosmological motivations to study UFDs: their presence constrains the small-scale behavior of dark matter models (e.g., Bullock & Boylan-Kolchin 2017; Kim & Peter 2021; Nadler et al. 2021), and their ages (~ 13 Gyr, e.g., Brown et al. 2014; Weisz et al. 2014) make them ideal candidates for being pristine relics from the era of reionization (e.g., Bovill & Ricotti 2009; Bland-Hawthorn et al. 2015; Weisz & Boylan-Kolchin 2017).

Additionally, despite having short periods of star formation histories (SFHs), UFDs with resolved metallicity dispersions

display significant internal spreads in stellar metallicity (e.g., Willman et al. 2011; Frebel et al. 2014). These observations suggest that they experienced complex chemical enrichment histories that distinguish them from star clusters (e.g., Willman & Strader 2012). Any complete theory of galaxy formation must be able to reproduce the properties of this population, and the small sizes of UFDs make them particularly sensitive to the specific implementation of physics in cosmological simulations (e.g., Munshi et al. 2019; Agertz et al. 2020).

Previous studies of the more luminous Local Group (LG) dwarf galaxies have demonstrated that well-populated metallicity distribution functions (MDFs) can be used to trace gas dynamics throughout their star formation histories (e.g., Tolstoy et al. 2009; Kirby et al. 2011, 2013, 2017; Ross et al. 2015; Jenkins et al. 2021). To learn about the physics of galaxy formation at the lowest-known masses to date, it is of great scientific interest to extend the availability of well-populated MDFs to the lower-luminosity UFDs. However, current spectroscopic studies have struggled to resolve metallicity dispersions in UFD candidates due to very few stars that are bright enough to be efficiently targeted, or observed at all, by current spectrographs (e.g., Martin et al. 2016; Walker et al. 2016; Li et al. 2018; Simon et al. 2020).



Original content from this work may be used under the terms of the [Creative Commons Attribution 4.0 licence](https://creativecommons.org/licenses/by/4.0/). Any further distribution of this work must maintain attribution to the author(s) and the title of the work, journal citation and DOI.

Although next-generation photometric surveys such as those from the Rubin Observatory are predicted to find many more UFDs at farther distances (e.g., Wheeler et al. 2019; Applebaum et al. 2021; Mutlu-Pakdil et al. 2021), spectroscopic facilities on future Extremely Large Telescope (ELT)-class telescopes may at best reach down to the sub-giant branch for Segue 1 luminosity UFD galaxies beyond 100 kpc (e.g., Figure 9 from Simon 2019).

One well-established alternative approach to measuring stellar metallicities is using medium or narrowband photometry (e.g., Strömberg 1966; McClure & van den Bergh 1968; Carney 1979; Geisler et al. 1991; Lenz et al. 1998; Karaali et al. 2005; Ross et al. 2013). Photometric filters are designed to target specific features in a star’s spectrum that are sensitive to intrinsic properties such as temperature or metallicity. Thanks to extensive calibration efforts, photometric metallicities are now used expansively to study the MW (e.g., Helmi et al. 2003; Ivezić et al. 2008; An et al. 2013; Cenarro et al. 2019; Huang et al. 2019; Arentsen et al. 2020; Youakim et al. 2020; Whitten et al. 2021; Chiti et al. 2021a), and can provide accurate metallicities for fainter stars than are accessible through spectroscopy.

One particularly useful photometric band for stellar metallicity is the calcium H&K (CaHK) doublet in the blue optical at 3968.5 and 3933.7 Å (e.g., Zinn 1980; Beers et al. 1985; Anthony-Twarog et al. 1991). More recently, the Pristine survey verified the promise for CaHK imaging around the CaHK feature to trace stellar metallicity for FGK stars (e.g., Starkenburg et al. 2017) and searched the MW for metal-poor stars (e.g., Youakim et al. 2017; Aguado et al. 2019; Venn et al. 2020). Subsequent ground-based imaging studies that leverage similar filters targeting CaHK features in MW satellites (e.g., Longeard et al. 2018; Han et al. 2020; Chiti et al. 2020; Longeard et al. 2021a) have demonstrated that this technique can substantially expand the sample of stars with metallicity measurements in these systems.

We extend this existing narrowband work in UFDs to even fainter stars and more distant galaxies using the Hubble Space Telescope (HST). Specifically, HST-GO-15901 (PI: D. Weisz) observed 18 UFD candidates in the F395N filter, which is analogous to the narrowband CaHK filter used by the Pristine survey. This paper is the first in a series based on these observations. Here, we demonstrate the power of HST CaHK imaging for uncovering the MDFs of UFDs using new and archival HST imaging of the MW satellite, Eridanus II (Eri II).

Eri II was initially discovered in Dark Energy Survey data by Bechtol et al. (2015) and Kposov et al. (2015). Subsequent deeper imaging by Crnojević et al. (2016) and Muñoz et al. (2018) confirm that at $M_V = -7.1$,¹³ Eri II is the faintest known galaxy to host a star cluster. Spectroscopic studies of Eri II by (Li et al. 2017, 16 stars on Magellan/Inamori-Magellan Areal Camera & Spectrograph (IMACS)) and (Zoutendijk et al. 2020, 26 stars on the Very Large Telescope/Multi Unit Spectroscopic Explorer (MUSE)) confirm that Eri II is a dark matter-dominated dwarf galaxy ($\sigma_{\text{vel}} = 6.9_{-0.9}^{+1.2}$ km s⁻¹) with a substantial internal spread in metallicity ($\langle [\text{Fe}/\text{H}] \rangle = -2.38 \pm 0.13$ and $\sigma_{[\text{Fe}/\text{H}]} = 0.47_{-0.09}^{+0.12}$; Li et al. 2017). SFH studies of Eri II, measured from HST broadband imaging (Simon et al. 2021; Gallart et al. 2021, and Alzate et al. 2021), show that its color–magnitude diagram (CMD) is consistent with having formed stars in a short burst (~ 100 Myr) that ended ~ 13 Gyr ago.

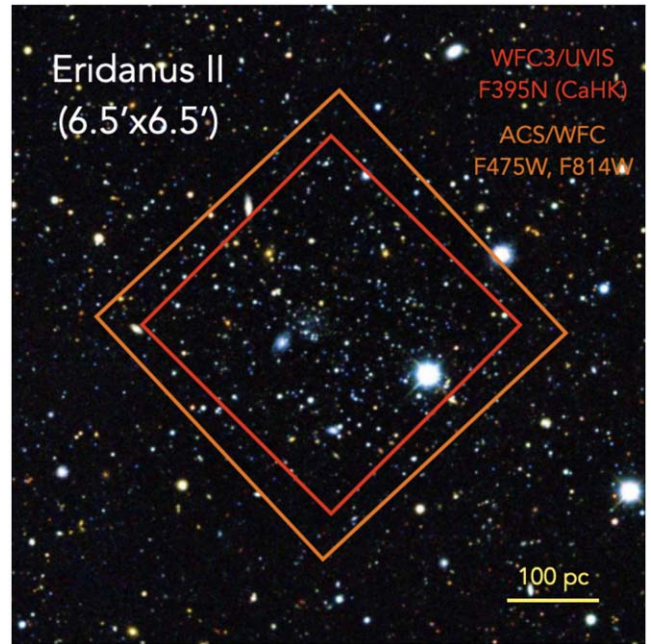


Figure 1. On-sky rendering of Eri II and our HST frames.

Eri II is ideal for demonstrating the efficacy of MDF inference from narrowband photometry. As the most luminous galaxy in our program, it not only provides a large sample of stars from which to measure a secure MDF, it also has a modest sample of spectroscopic metallicities, which is unusual for most UFDs, allowing us to cross check our findings.

In this paper, we combine HST Wide Field Camera 3 (WFC3)/Ultraviolet Imaging Spectrograph (UVIS) imaging of Eri II in the narrowband F395N filter with broadband archival HST photometry to measure metallicities for 60 stars in Eri II. In Section 2, we describe our observations and data reduction process. In Section 3, we describe our process for translating our data into metallicity measurements. In Section 4, we present the resulting MDF of Eri II, as well as analytic fits. In Section 5, we discuss our results in the broader context of galaxy formation and cosmology. We conclude with forward-looking remarks in Section 6.

2. Data and Observations

2.1. Photometry

We observed Eri II using HST on 2020 February 19 as part of HST-GO-15901 (PI: D. Weisz) using the WFC3/UVIS camera and in the F395N narrowband filter for two orbits. We performed small dithers to remove hot pixels and reject cosmic rays, choosing patterns that were used to measure proper motions of nearby galaxies from previous Treasury program HST-GO-14734 (PI: N. Kallivayalil). In this study, we also used spatially overlapping archival Advanced Camera for Surveys (ACS)/WFC F475W and F814W broadband imaging of Eri II, taken as part of HST-GO-14224 (six orbits; PI: C. Gallart, Gallart et al. 2021).

Figure 1 shows the placement of our WFC3/UVIS imaging relative to Eri II and to the footprint of the archival ACS observations. At the distance of Eri II, the WFC3/UVIS and ACS/WFC imaging subtends ~ 290 and ~ 360 pc, respectively, across one side of the image. We also note that both frames

¹³ We note that the exact luminosity depends on the adopted distance of Eri II.

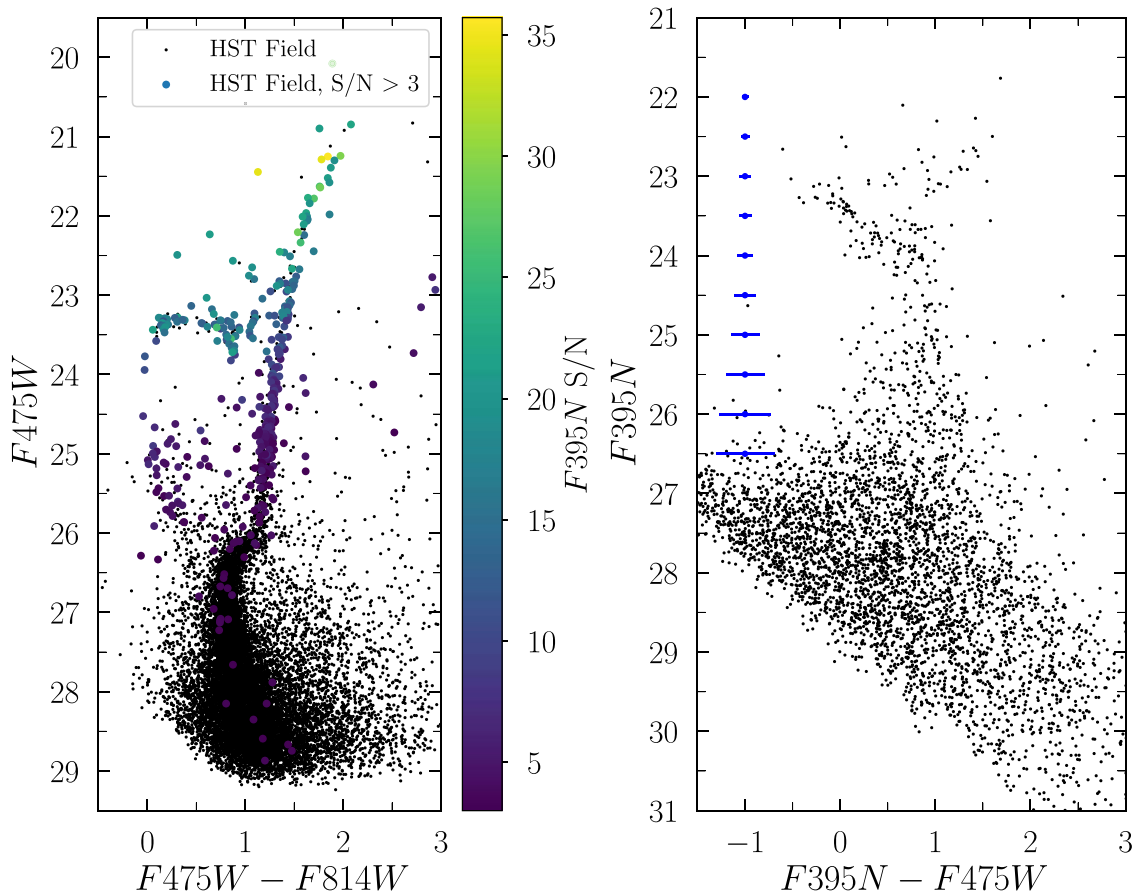


Figure 2. Left: the broadband CMD of the Eri II field population for stars that pass the quality cuts. We color code points with their corresponding S/N in F395N for S/N > 3. In this panel and the next, the photometry plotted excludes stars within two half-light radii of the galaxy’s cluster. Right: CMD of the Eri II field population with F395N. The blue error bars show the typical uncertainty as a function of F395N. Uncertainties on F395N–F475W color are dominated by F395N.

capture the star cluster of Eri II, which will analyze the cluster in a future paper.

We use DOLPHOT (Dolphin 2016, 2000) to perform point-spread function (PSF) photometry simultaneously on the F395N, F475W, and F814W *flc* images of Eri II. From the resulting catalog of objects recovered by DOLPHOT, we select stars by applying a quality cut to the deep broadband imaging. Specifically, we only include stars with S/N > 5, $|\text{sharp}|^2 < 0.3$ and $\text{crowd} < 1$ in each band.

Figure 2 shows the broadband CMD of stars that pass the quality cuts in each filter. Color-coded stars in the left panel are those with F395N S/N > 3. The right panel shows the F395N narrowband CMD. The blue error bars show the typical uncertainty in color as a function of F395N.

2.2. Selection of Stars for Photometric Metallicity Determination

We apply further cuts to select stars for our metallicity inference in Section 3, following the convention of past studies that use narrowband photometry of the CaHK lines to study the MDF of MW satellites. To begin, we select stars with F395N S/N > 10: this is the S/N threshold above which the photometric measurements can provide reliable metallicities (e.g., Longeard et al. 2018). We also remove any stars that fall within two half-light radii of the galaxy’s star cluster using the structural parameters provided by Simon et al. (2021) ($r_h \sim 0'.16$), as the focus of this paper is on the field population. From the resulting

sample, we limit our analysis to only stars that fall along the red giant branch (RGB) of Eri II. We exclude horizontal branch stars in the galaxy that also have sufficient S/N in F395N because the wavelength region of the narrowband filter is dominated by the Balmer lines in these hot stars, rather than the metallicity sensitive H&K lines (e.g., Starkenburg et al. 2017).

The left panel of Figure 3 presents the final sample of stars that we use for our analysis. The orange box on the broadband CMD indicates the box used to select the final sample of stars. These 60 stars have F395N S/N ranging from ~ 10 –36. We verify that the star at F475W ~ 20.8 and F475W – F814W ~ 2.0 , which falls right above the selection box, is brighter than the tip of the red-giant branch (TRGB) of a metal-poor isochrone shifted to the distance modulus of Eri II from Crnojević et al. (2016) and reported in Table 1, and therefore exclude it from our analysis.

The center panel of Figure 3 shows where our sample falls on the Sloan Digital Sky Survey (SDSS)-Pristine color space defined by the Pristine survey, and which was derived from a similar color space defined by Keller et al. (2007) for the Skymapper survey. Starkenburg et al. (2017) demonstrated that the color space $(g_{\text{SDSS}} - i_{\text{SDSS}})^{14}$ versus $(\text{CaHK} - g_{\text{SDSS}}) - 1.5(g_{\text{SDSS}} - i_{\text{SDSS}})$ was effective for separating stars of different metallicities. For our study, we use the equivalent HST filters F395N, F475W, and F814W to construct an analogous color space where the x -axis is defined as F395N–F475W, and the y -axis

¹⁴ Technically, Starkenburg et al. (2017) apply the extinction correction to their data, whereas we apply extinction to the model as described in Section 3.

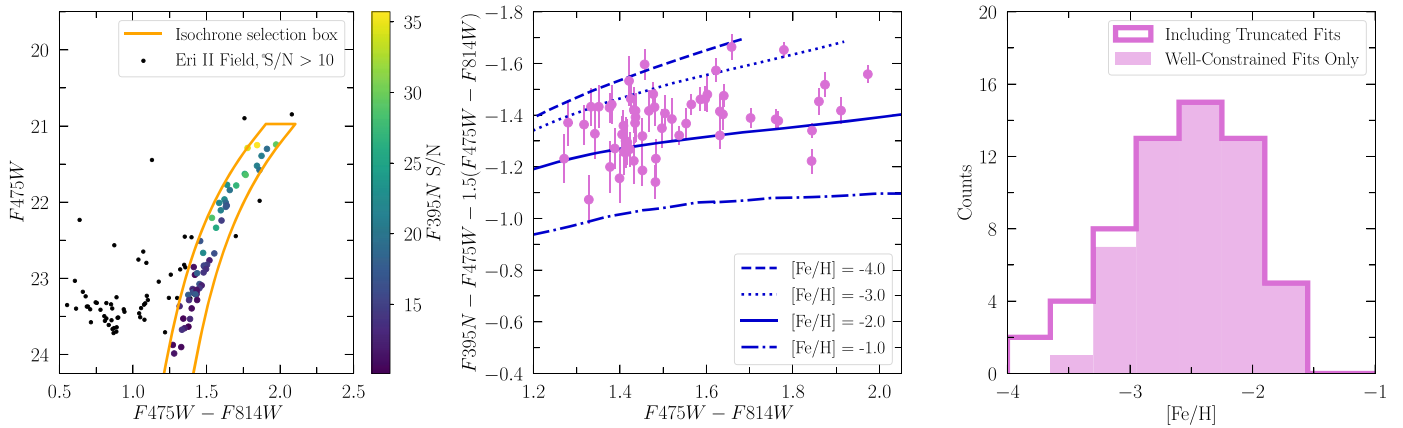


Figure 3. Left: broadband CMD of Eri II. Black points are photometry with F395N S/N > 10. The orange outline is the box that we used to select RGB stars in Eri II for our MDF analysis, and the color-coded points are the 60 selected stars. Our final sample reaches past the horizontal branch of Eri II. Center: the sample of Eri II stars that we use for our MDF analysis, plotted in the CaHK photometry color space defined by Starkenburg et al. (2017). We also apply extinction in the line of sight of Eri II to the MIST mono-metallic isochrone tracks for 13 Gyr stellar populations with $[\alpha/\text{Fe}] = +0.4$. We plot these tracks here to demonstrate how they separate in this particular color space. Right: MDF of Eri II, constructed from point estimates. Bin sizes are the median uncertainty of Eri II metallicity measurements (0.35 dex). The outlined histogram includes point metallicity estimates of stars whose posterior distributions describe an upper limit on metallicity due either to model limitations or S/N, which we elaborate on in Section 4.

Table 1
Properties of Eri II

Parameter	Eri II
R.A. (h:m:s)	03:44:20.1 \pm 10 ⁷ .5
Decl. (d:m:s)	-43:32:0.1 \pm 5 ⁷ .3
Distance modulus (mag)	22.8 \pm 0.1
Distance (kpc)	366 \pm 17
Absolute magnitude (M_V)	-7.1
Luminosity (L_\odot)	6 \times 10 ⁴
Eccentricity (ϵ)	0.48 \pm 0.04
Half-light radius (')	2.3 \pm 0.12
Half-light radius (pc)	277 \pm 14

Note. Structural parameters of Eri II, derived from Crnojević et al. (2016).

of this space is defined as $(F395N - F475W) - 1.5(F475W - F814W)$. We henceforth refer to the y-axis color as the CaHK color index, and to the entire color space as the CaHK color space. As shown in the center panel of Figure 3, the synthetic HST photometry from Modules for Experiments in Stellar Astrophysics (MESA) Isochrones and Stellar Tracks (MIST) isochrones (Choi et al. 2016; Dotter 2016) also separate in this space according to metallicity. We discuss the data, relative to these models, in Section 3.

2.3. Artificial Star Tests

We use artificial star tests (ASTs) to compute the uncertainties on our photometry. The procedure for an AST is as follows: we insert an artificial star with input magnitudes in F395N, F475W, and F814W onto a random position in the corresponding HST flc image. We only input stars whose broadband photometry fall within the isochrone selection box in the left panel of Figure 3, and with F395N photometry that fall within the CaHK color space in the middle panel of Figure 3.

We then attempt to recover the star in all of these photometric bands using the same PSF-fitting procedure and the same culling properties for our photometric measurements. Additionally, we require that ASTs are within

0.75 mag of their input magnitudes, which helps mitigate spurious blends. The output of an AST is the difference between the measured magnitude and the input magnitude (out-in). We perform 85,580 ASTs. This large sample allows us to quantify (i) average offsets in measured photometry (bias) and (ii) the variance of out-in (error) at all locations in the CaHK space. In Section 3, we describe how we apply the resulting error profile from ASTs to our metallicity inference.

3. Metallicity Measurements

The middle panel of Figure 3 shows the location of our 60 Eri II field RGB stars on the CaHK color-color plot. We overplot the alpha-enhanced ($[\alpha/\text{Fe}] = +0.40$), 13 Gyr MIST isochrones for giant stars. The models have been extinction corrected using the dust maps of Schlegel et al. (1998) and bolometric extinction corrections provided with the MIST models (Choi et al. 2016) which enable us to calculate the extinction for the F395N filter. We also consult the TRIdimensional model of the GALaxy (TRILEGAL) MW model (Vanhollebeke et al. 2009) to determine the extent to which contaminants would affect our sample: due to the small field of view and our particular CMD cuts, the chance that our sample contains contaminants are low. Moreover, the CaHK photometry of potential contaminants imply that they would likely be more metal-rich than $[\text{Fe}/\text{H}] > -1.0$, which we do not observe in our data. Finally, we also verify that none of the stars in our sample have been deemed Eri II nonmembers through spectroscopy (Li et al. 2017; Zoutendijk et al. 2020).

The majority of our sample lie between the $[\text{Fe}/\text{H}] = -3$ and $[\text{Fe}/\text{H}] = -1$ tracks, with a mean value somewhere between $[\text{Fe}/\text{H}] = -3$ and $[\text{Fe}/\text{H}] = -2$. Even by eye, it is apparent that the stars in Eri II span a range of ~ 2 dex in metallicity. This observation is robust for both the bright stars and the faint stars in our sample.

We derive metallicities for each star by first retrieving synthetic HST photometry for mono-metallic MIST isochrones; we use the MIST models for our analysis because it is the only currently available set of evolutionary models that

include stellar populations as metal-poor as $[\text{Fe}/\text{H}] = -4.0$.¹⁵ We limit our analysis to using tracks only for a 13 Gyr stellar population, in accordance with the SFHs of Eri II from broadband HST data (i.e., Gallart et al. 2021; Simon et al. 2021, and Alzate et al. 2021). We obtained advance access to the MIST v2 models, which are the alpha-enhanced version of the MIST v1 models. We use these models, instead of solar-scale alpha models, to fit Eri II because UFDs with short bursts of star formation are generally expected to have enhanced alpha element abundances over a large range of their stellar metallicities (e.g., Vargas et al. 2013; Frebel et al. 2014). We refer readers to Appendix A for additional discussion on the impact of alpha enhancements.

Next, we apply the results of the ASTs to each mono-metallic model. For each mono-metallic isochrone, we match each model isochrone point to its closest set of AST input magnitudes. From those ASTs, we calculate the bias and apply it to each isochrone point as offsets. We find for the ASTs that the CaHK color index has a positive color bias that increases for lower S/N points. A star with $F475W - F814W = 1.4$ and a CaHK color index of -1.0 , corresponding to a point on the lower RGB of Eri II, would have a color bias of $+0.1$ in CaHK. In contrast, a star with $F475W - F814W = 1.8$ and a CaHK color index of -1.3 , corresponding to the upper RGB of Eri II, would have a color bias of $+0.025$ in CaHK. As a result, all of the isochrone tracks are shifted redward in CaHK space, though based on the spacing between the tracks and the S/N of our data, they do not result in drastically different metallicities. This bias effect is driven by the shallower F395N observations, and may arise from charge transfer efficiency corrections and/or post-flash effects on the photometry that cause us to lose signal for fainter stars. We intend to investigate this issue in greater detail in future work.

After applying the bias from the ASTs, we apply extinction using the dust maps of Schlegel et al. (1998) and bolometric corrections from the MIST models (Choi et al. 2016). Once we apply the instrumental error profile and extinction models to the synthetic photometry, we linearly interpolate the CaHK color index as a function of $F475W - F814W$ to allow for the evaluation of the model at any color value.

As the middle panel of Figure 3 shows, the uncertainty in $F475W - F814W$ color of each star is small compared to the uncertainty in the CaHK color index. While the largest uncertainty in $F475W - F814W$ is ~ 0.01 mag, the uncertainty in the CaHK color index is at least 0.03 mag for the highest S/N points, and 0.1 mag for the lowest S/N. For simplicity in our fitting, we assume that the error in the $F475W - F814W$ color is negligibly small. We verify that scatter from the ASTs at a given CaHK location are statistically identical to the photometric errors reported by DOLPHOT. For simplicity, we adopt the photometric errors reported by DOLPHOT for our analysis.

For each star, we hold its $F475W - F814W$ color as constant and compute the corresponding model CaHK photometry at every metallicity using the tracks interpolated from MIST. To measure the metallicity of an individual star, we adopt a

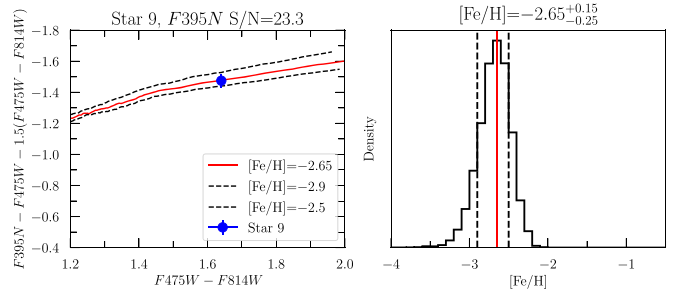


Figure 4. Example of a star (Star 9) with a well-constrained metallicity posterior distribution. (Left) The location of Star 9 in CaHK color space, plotted with the MIST isochrone models corresponding to the median, 16th, and 84th percentiles of its metallicity posterior distribution. (Right) The metallicity posterior distribution for Star 9.

Gaussian likelihood function of the form:

$$\log L = -\frac{1}{2} \frac{(\text{CaHK} - \text{CaHK}_m([\text{Fe}/\text{H}]))^2}{(\sigma_{\text{CaHK}}^2)}, \quad (1)$$

where CaHK and σ_{CaHK} are the corresponding CaHK color index measurement and measurement uncertainty, and $\text{CaHK}_m([\text{Fe}/\text{H}])$ is the model CaHK color index corresponding to a particular metallicity at a fixed $F475W - F814W$ color. We adopt uniform priors on metallicity over the range of the grid that includes the star’s $F475W - F814W$ color. We sample the resulting posterior distribution using *emcee* (Foreman-Mackey et al. 2013) by initializing 50 walkers and running the Markov Chain Monte Carlo chain for 10,000 steps, with a burn-in time of on average 50 steps per star. We monitor for convergence using the Gelman–Rubin statistic (Gelman & Rubin 1992).

We present sample metallicity fits for individual stars in Appendix B and the table of metallicity measurements in Table 3.

4. Results

4.1. Individual Measurements

In the right panel of Figure 3, we present the MDF of Eri II. The reported metallicities are the median of the marginalized posterior distribution for each star. Table 3 lists the median and 68% confidence interval for each star. Metallicity uncertainties are typically on the order of 0.1 dex, though they vary depending on the SNR, metallicity of the star, and location on the RGB, as we discuss below.

Our MDF of Eri II has a peak between -2.5 and -2.0 . It spans a range of at least 2.0 dex: as we discuss below, some of the most metal-poor stars are consistent with metallicities lower than what our model grid allows. We also present our measurements in Table 3, and now discuss features in the posterior distributions of our metallicity measurements.

Figure 4 presents an example of a star with a well-constrained metallicity posterior distribution. A well-defined metallicity posterior distribution has a clear peak and clear tails, and are narrower for higher S/N stars. Metallicity posterior distributions also tend to have longer metal-poor tails because the CaHK models are less distinguishable at the metal-poor end (e.g., middle panel of Figure 3). We present additional examples in Figure 12 in Appendix B.

¹⁵ We recognize that there are known issues with the performance of MIST/MESA isochrones for metal-poor stars (see, e.g., Kieley et al. 2021, and references therein), and that refining the models of metal-poor stars remains an active area of research (e.g., Karovicova et al. 2020). However, as we show in Section 4, the metallicities we derive using MIST are consistent with other Eri II metallicity measurements in the literature. We deem this result sufficient for this paper in demonstrating the power of CaHK photometry to recover broad features of the MDF of Eri II.

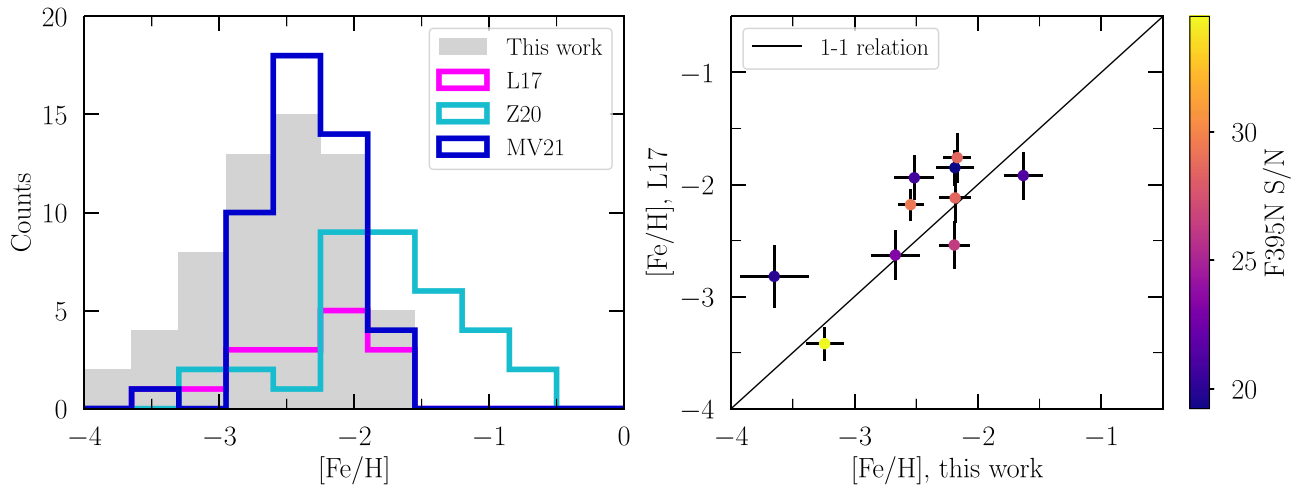


Figure 5. Results of fitting the metallicities of individual stars to CaHK photometry. Left: histogram of point measurements from this work, compared with those from L17, Z20, and MV21. Bin sizes are the median uncertainty of Eri II metallicity measurements (0.35 dex). Right: 1–1 comparison of our measurements with those from L17 for the 10 stars common to both of our samples.

There are three stars for which we derive only upper limits on the metallicity. These are stars with high S/N in F395N ($S/N > 15$) and whose photometry places them at the edge or beyond the grid of models that we use to make our metallicity inference. We flag these stars as candidate extremely metal-poor stars (EMP; $[\text{Fe}/\text{H}] < -3.0$) that may be of interest for future spectroscopic studies, and discuss them in more detail in Section 4.5. We also present the posterior distributions of these stars in Figure 13.

There are 10 stars in our sample whose photometric error bars fall within 1σ of the metal-poor grid edge, but whose metal-poor posterior distribution truncates within 2σ ; we also note these stars in Table 3. It is possible that at least some of these stars are more metal-poor than the value that we report, and that the measurements we derive here are limited by the models that we use. We provide posterior distributions of these stars in Figure 14. In the same vein, there are four stars whose 1σ error bars are at the edge of our grid, meaning that their posterior distributions show a clear peak, but the metal-poor tail is even more truncated.

Finally, there are four stars for which we report only an upper limit because of their low S/N photometry ($S/N \sim 10$). These are stars whose posterior distributions show no clear peak.

4.2. Comparison to Literature

In this section, we compare our MDF of Eri II to those currently in the literature: Li et al. (2017), Zoutendijk et al. (2020), Gallart et al. (2021), and Martínez-Vázquez et al. (2021), henceforth L17, Z20, G21, and MV21, respectively. L17 and Z20 target RGB members of Eri II using spectroscopy and obtain metallicity measurements for some of the same stars in our sample. From these studies, we can directly compare individual measurements using different methods to evaluate the efficacy of CaHK metallicities. In contrast, for G21 and MV21, we cannot do star-by-star comparisons, but we can compare the overall MDF derived from the various methods. G21 uses deep HST photometry to measure the SFH of Eri II, inferring an MDF in the process. MV21 studies variable stars in Eri II, and measures the galaxy’s MDF from its RR Lyrae stars.

We first discuss how our metallicity measurements compare against the spectroscopic studies. For context, L17 targeted

candidate Eri II members within $8'$ of the galaxy using Magellan/IMACS spectroscopy. They report metallicities derived using the calcium triplet (CaT) equivalent width calibration (Carrera et al. 2013) for 16 RGB members of Eri II, down to a magnitude of $g_{\text{DES}} \sim 21.7$ mag. Z20 targeted candidate Eri II members within $1'$ centered on Eri II using VLT/MUSE spectroscopy. They report metallicities derived using full-spectrum fitting with the PHOENIX model spectra (Husser et al. 2013) for 26 Eri II member stars, down to a magnitude of $F606W \sim 23.8$ mag.

In Figure 5, we compare our measurements against those of L17 and Z20. The histogram in the left panel compares our MDF with those from L17 and Z20. The right panel compares our metallicity measurements with the 10 common stars we have with the L17 sample.

We find good agreement between our metallicities and those in L17: while the scatter is a little larger than expected from the reported uncertainties, there is no evidence of a systematic offset between the two studies. In contrast, we find disagreement with the results of Z20. Z20 find systematically more metal-rich stars and report systematically smaller uncertainties. The MDF of Z20 implies that Eri II would be a more metal-rich system than implied by the dwarf galaxy luminosity-metallicity relationship (L17; see Section 5). Z20 noted a similar disagreement with L17, but did not explore the origin of this tension. Resolving this issue is beyond the scope of this paper.

Next, we compare our results against those from the photometric studies. G21 studied the SFH of Eri II from deep HST broadband data and inferred an MDF for the galaxy as part of their work. While their MDF spans the same metallicity range as ours, the shape is qualitatively different from the one that both we and MV21 (below) derive. Given the differences in the technique and the part of the CMD used to infer the metallicities, it is challenging to discern the source of discrepancy.

MV21 studied RR Lyrae stars in Eri II using multi-epoch g , r , and i imaging on the Goodman and Dark Energy Cameras, as well as F475W, F606W, and F814W from HST/ACS. They derive metallicities from 46 RR Lyrae stars using the period–luminosity relations from Cáceres & Catelan (2008) and Marconi et al. (2015).

The left panel of Figure 5 compares our MDF against those derived from the RR Lyrae sample in MV21. The peak of our MDF is consistent with that of MV21, though we are able to recover more metal-poor stars. This discrepancy may be expected from using different populations of stars to trace the MDF: MV21 point out that stars in the metal-poor tail of the MDF may not fall into the instability strip as RR Lyrae stars. As a result, MV21 also recover a smaller metallicity dispersion ($\sigma_{[\text{Fe}/\text{H}]} = 0.3$ dex) compared to what we derive in Section 4.3 ($\sigma_{[\text{Fe}/\text{H}]} = 0.42$ dex).

Overall, these comparisons suggest that our metallicity measurements can recover results that are consistent with those from the literature.

4.3. Gaussian MDF Fit

Following long-standing practice in spectroscopic studies of UFDs (e.g., Willman & Strader 2012; Kirby et al. 2015; Li et al. 2018; Simon et al. 2020), we fit a Gaussian to the MDF of Eri II.¹⁶ In particular, we use the two-parameter Gaussian likelihood function used by L17, which was adapted from Walker et al. (2006):

$$\log L = -\frac{1}{2} \sum_{i=1}^N \log(\sigma_{[\text{Fe}/\text{H}]}^2 + \sigma_{[\text{Fe}/\text{H},i]}^2) - \frac{1}{2} \sum_{i=1}^N \frac{([\text{Fe}/\text{H}]_i - \langle [\text{Fe}/\text{H}] \rangle)^2}{\sigma_{[\text{Fe}/\text{H}]}^2 + \sigma_{[\text{Fe}/\text{H},i]}^2}, \quad (2)$$

where $\langle [\text{Fe}/\text{H}] \rangle$ and $\sigma_{[\text{Fe}/\text{H}]}$ are the mean metallicity and metallicity dispersion of Eri II, and $[\text{Fe}/\text{H}]_i$ and $\sigma_{[\text{Fe}/\text{H},i]}$ are the metallicity and metallicity uncertainties for each star. We assume uniform priors on the mean, with the maximum and minimum set by the range of the point metallicity measurements, and require that the metallicity dispersion be greater than zero ($\sigma_{[\text{Fe}/\text{H}]} > 0$). We use `emcee` to sample the posterior distribution, initializing 50 walkers for 10,000 steps. The autocorrelation time for this run is 30 steps. The GR statistic indicates that the chains are converged.

For stars with different lower and upper uncertainties measured from the 16th and 84th percentiles of their probability density functions (PDFs), we adopt the average of the error bars to use in our fit. For stars that have only upper limit constraints, we include them in our fit using the medians of their PDFs as the point estimate and 16th/84th percentiles values to compute uncertainties. All of these are approximations, and in principle, a more rigorous approach would be to use individual PDFs in our MDF inference. We will consider such an approach in subsequent papers in this series.

From 60 stars, we measure a mean metallicity of $-2.50^{+0.07}_{-0.07}$ dex and metallicity dispersion of $0.42^{+0.06}_{-0.06}$ dex. We present the resulting joint distribution in the Appendix D as Figure 16, and tabulate these values in Table 2.

In comparison, L17 measure a mean metallicity of -2.38 ± 0.13 dex and a metallicity dispersion of $0.43^{+0.12}_{-0.09}$. Thus, using a completely independent approach to measuring the MDF, we find consistency with and improved precision over the CaT MDF. Beyond enabling a precise measurement of

¹⁶ Although, we note that studies such as Leaman (2012) suggest that the MDFs of dwarf galaxies are not well represented by a Gaussian form. We will explore this further in a study of the full galaxy sample.

Table 2

Parameters of Analytic MDF Fits to Eri II for the Gaussian, Leaky Box, Pre-enriched Gas, and Accretion Models

Model	Parameters	Values
Gaussian	[Fe/H]	$-2.50^{+0.07}_{-0.07}$
	$\sigma_{[\text{Fe}/\text{H}]}$	$0.42^{+0.06}_{-0.06}$
Leaky box	p_{eff}	$0.005^{+0.001}_{-0.001}$
	AICc	96.04
Pre-enriched	p_{eff}	$0.004^{+0.001}_{-0.001}$
	$[\text{Fe}/\text{H}]_0$	$-3.73^{+0.21}_{-0.17}$
	ΔAICc	-1.06
Accretion	p_{eff}	$0.005^{+0.001}_{-0.001}$
	M	$2.77^{+2.59}_{-1.14}$
	ΔAICc	-0.04

Note. We report the AICc for the leaky box, and for the pre-enriched gas and accretion models, we report the difference in AICc between those models and that of the leaky box.

the MDF of Eri II, this finding also demonstrates the power of CaHK imaging in practice.

4.4. Analytic Chemical Evolution Models

The MDF of a galaxy is shaped by the gas dynamics throughout the course of its SFH. One-zone chemical evolution models are simple analytic MDFs that have long been used for interpreting the formation process of various MW components (e.g., Schmidt 1963; Lynden-Bell 1975; Pagel & Patchett 1975; Hartwick 1976; Tinsley 1980), as well as those of its nearby dwarf galaxies (e.g., Helmi et al. 2006; Kirby et al. 2013; Ross et al. 2015).

Prior to this work, the only UFD whose MDF was sufficiently populated enough to fit one-zone chemical evolution models is Bootes I, which has been analyzed by Jenkins et al. (2021), Romano et al. (2015), and Lai et al. (2011). In this section, we follow precedent set by the aforementioned studies by fitting the leaky box, pre-enriched, and accretion/extra gas chemical evolution models to the MDF of Eri II.

The leaky box model defined by Pagel (1997) describes the scenario where a galaxy forms stars from gas that is initially devoid of metals, and loses gas in the process of successive star formation and enrichment. Its single parameter is p_{eff} , the effective yield, which encapsulates contributions from both supernova enrichment and gas outflow to the stellar MDF.

The pre-enriched model and the accretion/extra gas models are more complex versions of the leaky box. The pre-enriched model assumes that star formation starts from pre-enriched gas of metallicity $[\text{Fe}/\text{H}]_0$. As a result, it imposes a floor on the lowest metallicity stars in the galaxy, and simplifies to the leaky box in the limit of $[\text{Fe}/\text{H}]_0 \rightarrow -\infty$. The accretion/extra gas model of Lynden-Bell (1975) describes a system that is allowed to accrete pristine gas during the process of star formation. This model adds an extra parameter, M , which is the final stellar mass in terms of the initial gas mass at the onset of star formation. An accretion model with $M > 1$ implies that the galaxy experienced accretion during its SFH, resulting in an MDF with a larger peak and a smaller metal-poor tail. When $M = 1$, the accretion model reduces to the leaky box.

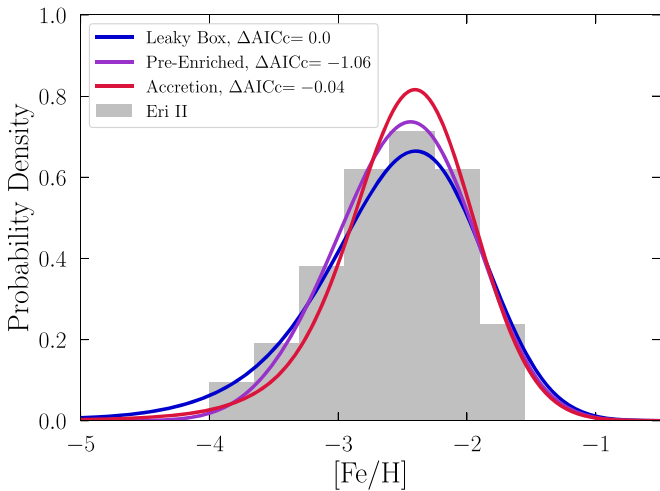


Figure 6. Comparing histogram of Eri II measurements to best-fit one-zone chemical evolution models. Bin sizes are the median uncertainty of Eri II metallicity measurements (0.35 dex), and the one-zone models have also been convolved with a Gaussian of the same width.

We find the best-fit parameters for these analytic MDFs following Jenkins et al. (2021) and Ji et al. (2021).¹⁷ Briefly, we adopt the Gaussian likelihood from Kirby et al. (2011) and Kirby et al. (2013), i.e., the likelihood for each star i is the convolution between the MDF and a Gaussian with standard deviation corresponding to that star’s metallicity uncertainty $\sigma_{[\text{Fe}/\text{H}],i}$ evaluated at the observed metallicity $[\text{Fe}/\text{H}]_i$. We treat error bars in our sample the same way as for the Gaussian MDF fit described in the previous section.

We use dynamic nested sampling with *dynesty* (Speagle 2020) to sample the parameters’ posterior distribution. We use fairly wide priors: log-uniform for p_{eff} from 10^{-3} to $10^{-1.1}$; uniform in $[\text{Fe}/\text{H}]_0$ from -4 to -2 for the pre-enriched model; and uniform in M from 1 – 30 for the accretion model.

We present the posterior distributions in Appendix D, and tabulate fit parameters in Table 2. We report the median of the posterior distributions for each parameter, and compute error bars using the 16th and 84th percentiles. For the pre-enriched model, the posterior distribution of $[\text{Fe}/\text{H}]_0$ is truncated at the metal-poor end. For the accretion model, the posterior distribution of M shows that our data can constrain an upper limit on M , but cannot rule out $M = 1$ with high confidence.

We present the best-fit MDFs in Figure 6. By eye, it looks that all models fit the MDF of Eri II reasonably well, and so we investigate whether the Eri II data prefer an MDF more complex than a leaky box. One way to quantify the model comparison is by using the corrected Akaike information criterion (AICc; Kirby et al. 2011), which is a penalized likelihood ratio test. We compute this statistic for the leaky box, pre-enriched, and accretion models. We tabulate the AICc for the leaky box in Table 2, and for the other two models, their difference in AICc ΔAICc from that of the leaky box. A positive value for ΔAICc would suggest that the model is preferred over the leaky box, but we find that there is no strong preference between the three models that we fit since the ΔAICc is small. *dynesty* also computes the Bayesian evidence, which we choose not use here as it is sensitive to the exact prior volume choice, but it provides similar conclusions as the AICc.

We now discuss limitations in our methodology that could change the analytic chemical evolution model interpretation. As we lay out in the previous subsection, we approximate the posterior distribution of measurements for individual stellar metallicities as Gaussian, despite posterior distributions having longer metal-poor tails due to the indistinguishability of CaHK metallicities in metal-poor regimes. As a result, our current methodology downweights the metal-poor tail of the MDF of Eri II. Fitting analytic models using the full PDFs of individual stellar metallicities would remedy this issue, and could bring the MDF of Eri II closer to the leaky box model.

Additionally, we caution that the one-zone models used in this work oversimplify the problem by assuming that galaxies quench via turning the last of its available gas into stars. This assumption is likely incorrect because star formation is rarely that efficient, and low-mass galaxies can be quenched via reionization, ram pressure stripping, and/or SNe feedback (see Eggen et al. 2021 for example of a $10^5 L_{\odot}$ galaxy in the field at $z=0$ that has been observed to experience SNe feedback, and also the discussion in Section 5). While one way to remedy this issue in future work would be to fit models that truncate star formation at a particular metallicity (see, e.g., the ram pressure stripping model from Kirby et al. 2013), additional detailed modeling would be fruitful for developing intuition around interpreting various components of a UFD’s MDF.

With the above caveats and the minimal differences in AICc between the three models in mind, we also note that the results of our pre-enriched and accretion fits suggest that they are also consistent with the leaky box limit. We therefore suggest that within the scope of our analysis in this work, the MDF of Eri II is best represented by the leaky box model, and discuss the implications in Section 5.

4.5. Noteworthy Individual Stars

Direct descendants of the first stars (Pop III) are hypothesized to be more easily identifiable in UFDs, owing to these systems’ comparatively simpler enrichment histories in contrast to those of their more luminous counterparts (e.g., Ji et al. 2015). The chemical abundances of EMPs in UFDs are of great scientific interest because they are thought to trace directly back to past rare chemical enrichment events (e.g., Ji et al. 2016) or to SNe ejecta from Population III stars (e.g., Frebel & Norris 2015; Jeon et al. 2017). In this section, we discuss the pathfinding potential for CaHK photometry to contribute to the search for these stars.

In Figure 7, we highlight spectroscopically accessible stars that are at the metal-poor edge of our fitting grid, that may be particularly enlightening for spectroscopic follow-up observations. In particular, we identify three stars that are candidate EMPs. As shown in Figure 13, these stars have truncated metal-poor posterior distributions, so they may be more metal-poor than our grids allow. They are also located on the upper RGB of Eri II, with the faintest star being $m_{\text{F475W}} \sim 22.5$ mag. Although their CMD position on the blue edge of the RGB raises the possibility that they are asymptotic red giant branch (AGB) stars, the purely ancient stellar population of Eri II (~ 13 Gyr) suggests that it is unlikely to have many, or any, AGB stars.

Of these three stars, two of them have CaT metallicities measured by L17. For Star 2 ($m_{\text{F475W}} = 21.3$, F395N S/N = 34.5), we find that it has $[\text{Fe}/\text{H}] = -3.50 \pm 0.15$,

¹⁷ Code available at <https://github.com/alexji/mdfmodels>.

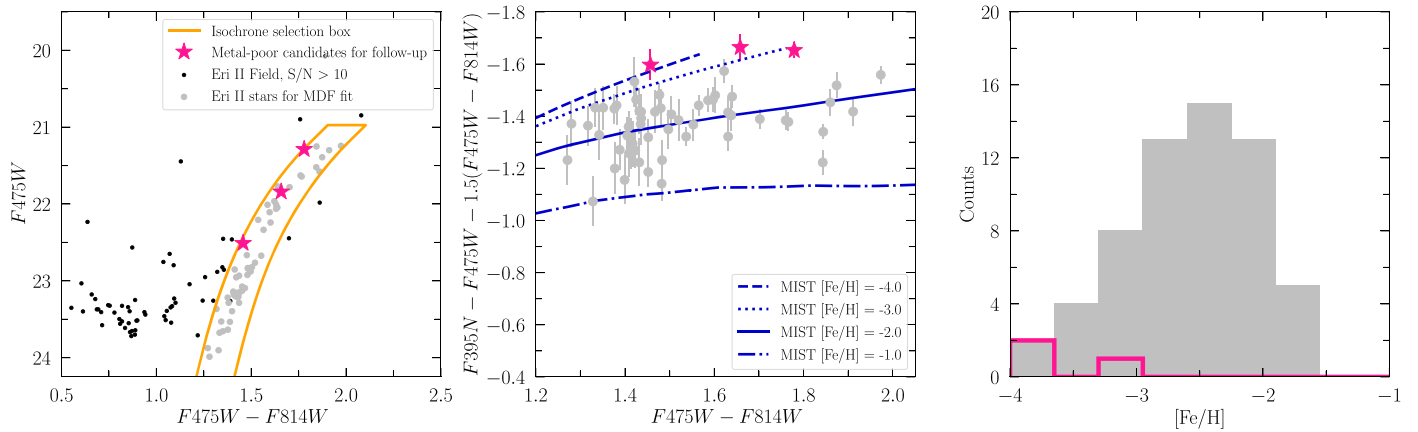


Figure 7. Left: CMD of Eri II RGB stars, highlighting the metal-poor star candidates (blue) that we discuss in Section 4.5 as being potential candidates for spectroscopic follow-up. Center: location of these stars in CaHK color space. Right: histogram demonstrating the contribution that these stars make to the MDF of Eri II. Bin sizes are the median uncertainty of Eri II metallicity measurements (0.35 dex).

compared to the L17 measurement of $[\text{Fe}/\text{H}] = -3.42 \pm 0.15$: these measurements are in good agreement with each other. For Star 11, we obtain a 95% upper limit of $[\text{Fe}/\text{H}] = -3.15$, compared to the L17 metallicity of $[\text{Fe}/\text{H}] = -2.82 \pm 0.28$. For these two stars, both our measurements and measurements from the literature affirm that they are consistent with having $[\text{Fe}/\text{H}] < -3.0$, demonstrating the potential for CaHK to identify EMP candidates. Additional spectroscopic observations could aim to ascertain the behavior of α element and C abundances in Eri II at low metallicities, which in turn can be used to infer the properties of the SNe whose yields contributed to these patterns (α , Nagasawa et al. 2018; Ji et al. 2020; C, Jeon et al. 2021).

Unlike the other two EMP stars that we identify, Star 21 ($m_{F475W} = 22.5$, $F395N\text{S}/N = 17$) does not have spectroscopic data. We estimate the upper limit of its metallicity to be $[\text{Fe}/\text{H}] = -3.05$. Additional observations to measure metallicities from CaT spectroscopy or full spectral fitting would be fruitful both for verifying that it is an EMP, as well as measuring its other chemical abundances.

4.6. Searching for a Metallicity Gradient in Eri II

Radial metallicity gradients have long been observed in LG dwarf spheroidal galaxies (e.g., Held et al. 1999; Harbeck et al. 2001; Saviane et al. 2000, 2001; Tolstoy et al. 2004; de Boer et al. 2012; Kacharov et al. 2017). The physics responsible for the origin and steepness of these gradients remain an active area of research, with proposed mechanisms such as natal angular momentum (e.g., Schroyen et al. 2011), stellar feedback (e.g., El-Badry et al. 2016), and SFHs (e.g., Mercado et al. 2021). To date, however, studies of metallicity gradients in dwarf galaxies have mostly been limited to those more luminous than $10^5 L_{\odot}$ (e.g., Vargas et al. 2014; Ho et al. 2015).

Motivated by recent searches for metallicity gradients in UFDs (Chiti et al. 2021b; Longeard et al. 2021b), we search for a spatial trend in our data. We find none. This could be because (1) there is none, (2) our imaging, which covers $< 1 r_h$ of Eri II, is too limited in spatial extent to find one, and/or (3) the uncertainties on the metallicity measurements need to be smaller, if the gradient is weak but nonzero.

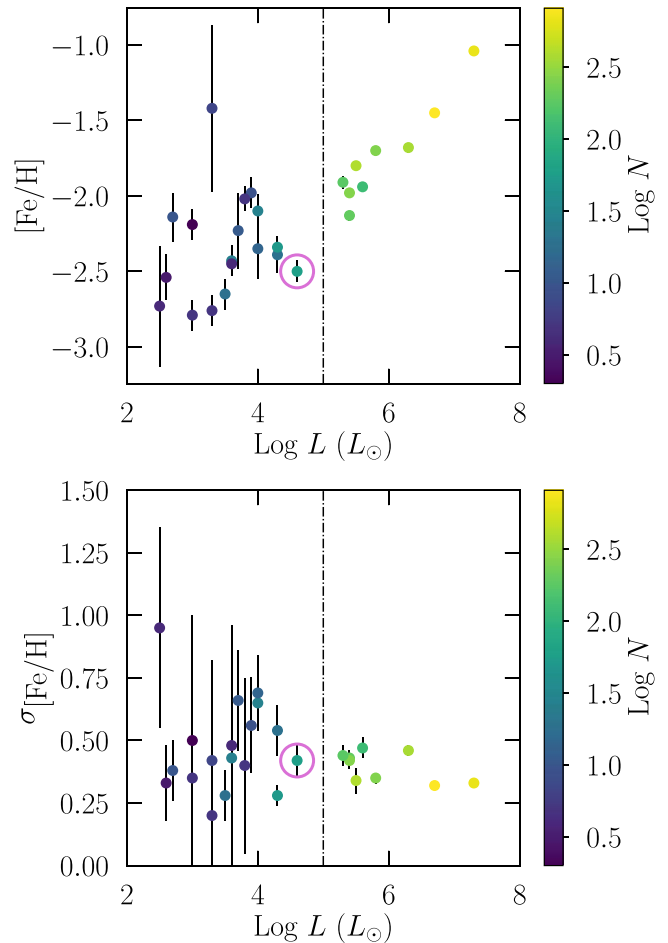


Figure 8. Subset of mean metallicity (top) and mean metallicity dispersions (bottom) for known MW satellites, color coded by number of stars used to make the measurement (compiled partly from Simon (2019), with updated measurements for Boo I from Jenkins et al. (2021) and including our Eri II measurement). The dashed-dotted line separates the ultra-faint dwarfs from the classical dwarfs. We indicate Eri II with the purple circle.

5. Discussion

5.1. Improved MDF Statistics for Eri II

Figure 8 compares the mean and σ from fitting a Gaussian to our MDF of Eri II with those derived for other LG dwarf

galaxies (data compiled by Simon 2019, with updated measurements for Boo I from Jenkins et al. 2021), where the data points are color coded by the number of stars used to measure the MDF in each system. The vertical line in both panels delineates the separation between UFDs and the classical dwarf galaxies as defined by Simon (2019). The top panel shows that the mean metallicity we derive for Eri II is fully consistent with its expected location along the mass–metallicity relationship for dwarf galaxies (Kirby et al. 2013). The bottom panel shows that the metallicity dispersion we derive is on a par with that of more luminous dSph galaxies, and within the range of dispersions observed so far in LG satellites. The agreement between our Eri II results and the broader dwarf galaxy MDF provides further support for the power of CaHK-based metallicities.

As discussed in Section 4.3, our MDF fit of Eri II provides a twofold increase in precision in metallicity dispersion over those of the measurements from L17 due to the expanded sample of stars with metallicity measurements. Out of all the UFDs with measured MDFs so far, Eri II is also now better characterized for the same reason: MDF measurements for other UFDs have been limited due to few stars that have been accessible through spectroscopic studies. These results affirm the potential for CaHK imaging to deliver improved UFD MDF statistics.

5.2. Quenching Mechanisms for Eri II

In this section, we address the questions around quenching mechanisms for Eri II. As part of this process, we derive the direct orbital history of Eri II following the methodology outlined in Patel et al. (2020), using updated Gaia eDR3 proper motions from McConnachie & Venn (2020a), the radial velocity from Li et al. (2017), and a distance consistent with that reported in Table 1.

Figure 9 summarizes the orbital history of Eri II in a low (MW1; $1 \times 10^{12} M_{\odot}$) and high mass (MW2; $1.5 \times 10^{12} M_{\odot}$) MW model. Orbits are computed in a MW-only (dashed lines), MW + LMC (solid lines), and a MW + Large Magellanic Cloud (LMC) + Small Magellanic Cloud (SMC); dotted lines) potential. We only integrate our orbits as far back as 6 Gyr because attempts to ascertain the orbital history of Eri II earlier than that will also need to account for the growth of the MW potential, and because orbital uncertainties become significantly larger beyond 6 Gyr ago.

In all scenarios, we find that Eri II is on first infall into the halo of the MW. Following Patel et al. (2020), we also account for the measurement uncertainties in proper motion, line-of-sight velocity (Li et al. 2017), and distance by computing 1000 orbits using Monte Carlo drawings of the joint uncertainties as initial conditions. Regardless of assumed MW mass, our models suggest that Eri II is statistically most likely to be on first infall as well (e.g., $\sim 98\%$ of all orbits result in the same orbital history). Moreover, we also verify that Eri II does not pass within 800 kpc of M31 at any point in its trajectory.

In summary, our updated orbit for Eri II suggests that it was isolated throughout most of its evolutionary history, though we caution that this orbital history is still informed by large uncertainties on the proper motion of Eri II. However, this result is also consistent with the results from Battaglia et al. (2021), who also derive an orbital history for Eri II using Gaia eDR3 proper motions and find that it is on first infall into the MW. The revised orbital history of Eri II from Gaia eDR3

proper motions is a departure from results of previous studies of Eri II, which suggested that Eri II has either completed multiple orbits around the MW (e.g., Li et al. 2017; Fritz et al. 2018) or is a backsplash galaxy (Buck et al. 2019). The discrepancies in these results are likely due to a combination of (1) different proper motion measurements between Gaia eDR3 and DR2 for Eri II,¹⁸ (2) orbit model-specific considerations (MW-only versus including the LMC), and (3) Calculating the past orbit of Eri II versus orbital history inference by following Eri II analogs in cosmological simulations.

We now turn to the question of how Eri II quenched. At the time of its discovery, Koposov et al. (2015) noted the presence of blue stars in the CMD of Eri II that suggest Eri II may have stopped forming stars only recently (~ 250 Myr ago). This scenario had also seemed viable because Eri II is ~ 380 kpc from the MW, and thus less likely to have experienced ram pressure stripping that could have removed gas before the suspected burst of recent star formation.

Subsequent studies, however, increasingly point away from this recent quenching scenario. Rodriguez Wimberly et al. (2019) study Eri II analogs in the Fat ELVIS simulations and find that it is unlikely for them to have quenched through infall into the MW halo. The orbital history of Eri II that we derive suggests that it fell into the MW only recently, which does not correlate with deep HST studies of Eri II suggesting that it formed the majority, if not all, of its stars before $z \sim 6$.

Finally, if Eri II was quenched through ram pressure stripping, we should expect to observe a sharp truncation in its MDF at the metal-rich end (e.g., the one-zone model of ram pressure stripping fit by Kirby et al. 2013), although accretion models with large M could also produce a similar feature. While our MDF does not uniquely rule out ram pressure stripping, it adds to the growing body of evidence in the literature pointing away from ram pressure stripping as a possible source of quenching for Eri II.

Beyond that, the interpretation of old SFH of Eri II is still up for debate. While Simon et al. (2021) interprets the SFH of Eri II as evidence of quenching by reionization, Gallart et al. (2021) suggests that SNe alone would be sufficient to quench Eri II. The MDF of Eri II that we derive does not provide definitive power to distinguish between these two mechanisms, as the one-zone models we fit do not distinguish between the details of how star-forming gas is depleted. However, any proper account of the physics driving star formation and quenching in Eri II should also be able to reproduce its large internal metallicity spread. Similar theoretical benchmarks are also set by observations of the Segue 1 UFD, a much fainter UFD ($M_V = -1.3$) that appears to have experienced a short burst of star formation, but whose stars span almost 2 dex in metallicity (Frebel et al. 2014).

5.3. Environmental Impacts on Dwarf Galaxy Evolution

In this section, we discuss the role of environment on dwarf galaxy evolution by comparing our results for Eri II to two other galaxies that are close to Eri II in luminosity, and which have published MDFs and one-zone chemical evolution model fits: Leo T and Boo I.

¹⁸ As an example to illustrate this, the east component of the proper motion changes of Eri II between DR2 (McConnachie & Venn 2020b) and DR3 (McConnachie & Venn 2020a) from $\mu_{\alpha} \cos \delta = 0.35_{-0.20}^{+0.21}$ mas yr⁻¹ to $\mu_{\alpha} \cos \delta = 0.21 \pm 0.09$ mas yr⁻¹ using the inference method that does not place prior expectations on the tangential velocity dispersion of the MW halo.

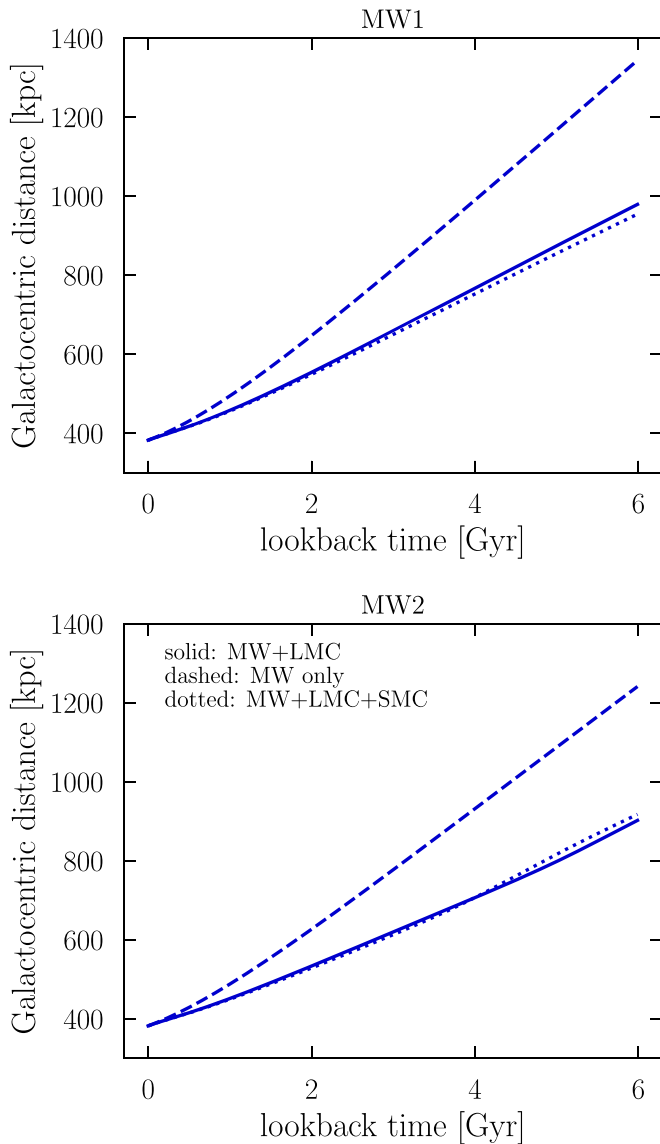


Figure 9. Orbital history of Eri II in two different MW mass potentials using Gaia eDR3 proper motions (McConnachie & Venn 2020a). MW1 has a virial mass of $10^{12} M_{\odot}$ while MW2 is more massive with a virial mass of $1.5 \times 10^{12} M_{\odot}$. Dashed lines represent orbits computed in a MW-only potential, solid lines indicate a MW+LMC potential with an LMC mass of $1.8 \times 10^{11} M_{\odot}$, and dotted lines represent a MW+LMC+SMC potential with an SMC mass of $5 \times 10^9 M_{\odot}$. All of the above scenarios illustrate that Eri II is on first infall into the MW’s halo.

Leo T is similar to Eri II in luminosity ($L \sim 4 \times 10^4 L_{\odot}$; Irwin et al. 2007) and distance ($d_{\text{MW}} \sim 410$ kpc; Clementini et al. 2012) from a more massive host. The key distinction between these two galaxies is that Leo T displays an extended SFH that continues past reionization (Clementini et al. 2012; Weisz et al. 2012), with a substantial reservoir of H I gas ($M \sim 2.8 \times 10^5 M_{\odot}$; Ryan-Weber et al. 2008), while Eri II stopped forming stars 13 Gyr ago. The orbital history of Leo T suggests that like Eri II, it also seemed to have evolved in isolation (Battaglia et al. 2021). Finally, similar to Eri II, the MDF of Leo T is best described by a leaky box (Kirby et al. 2013).

On the other hand, Boo I has a CMD which suggests that it underwent a similar SFH to Eri II: a short starburst that ended also around 13 Gyr ago (Brown et al. 2014). Unlike Eri II, the

orbital history of Boo I suggests that it is bound to the MW (Fritz et al. 2018; Simon 2018) and, as a result, possibly formed in a denser environment relative to that of Eri II.¹⁹ Finally, the MDF of Boo I is best represented by an accretion model (Jenkins et al. 2021), suggesting that the dense environment it was born in could have allowed it access to extra gas.

As a point of reference, Kirby et al. (2013) fit one-zone models to the MDFs of the more massive LG dwarf galaxies, and found that while the MDFs of dwarf spheroidal galaxies, which are bound to the MW, are better described by accretion models, the MDFs of isolated dIrrs are better described by leaky box or pre-enriched models. To the best of the data that we currently have for galaxies of lower luminosities, these distinctions between MDFs seems to also hold for UFDs that have long been bound to a more massive host versus UFDs that likely evolved in more isolated environments.

Instead of present-day morphology, Gallart et al. (2015) offer a framework for interpreting the role of environment in dwarf galaxy formation by classifying dwarf galaxies into *fast dwarfs* and *slow dwarfs* based on their SFH. *Fast dwarfs* are those with SFHs consisting of a single short, but dominant, event. *Slow dwarfs* show current or recent SFH, with continuous activity starting from the oldest epochs. Under this framework, distinctions in SFH arise from the environments in which the galaxies were forming stars: fast dwarfs formed in dense environments where they frequently experienced interactions that would result in rapid star formation (e.g., gas accretion, mergers) and its rapid truncation (e.g., feedback from SNe and reionization from within and from adjacent galaxies), while slow dwarfs formed throughout cosmic time in a lower-density environment far from the influence of massive hosts.

While the characteristics of Boo I and Leo T, respectively, fit into the fast dwarf and slow dwarf categories, Eri II complicates this picture: it resembles a fast dwarf on the basis of its short and early burst of SFH, but the updated orbit that we derive for Eri II and the similarity of its MDF to those of several other isolated dIrrs suggests that Eri II has largely evolved in isolated like slow dwarfs.

Using the SFH of Eri II, Gallart et al. (2021) argue that it is possible for Eri II to self-quench entirely through SNe feedback rather than reionizing radiation, e.g., from adjacent massive hosts. If this is the case, then UFDs with SFHs that would render them as fast dwarfs can also quench early, independent of environment. On the other hand, the similarity between the MDFs of Eri II and Leo T, and of some other isolated dIrrs, despite their different SFHs, raises the possibility of common formation pathways for fast and slow dwarfs that evolve in isolation.

We of course offer the above discussions with the caveat that they consider limited numbers of UFDs, and with results that would benefit from further refinement, e.g., the leaky box fit for Leo T was made using only 16 stars. In any case, this line of investigation could be furthered with studies of more UFDs. Here, the CaHK imaging technique will also be useful, as it will allow us access to stellar metallicities of the less luminous and more distant galaxies currently known (e.g., Andromeda XVI, as part of HST-GO-16686; PI: D. Weisz), and that are expected to be discovered in upcoming surveys.

¹⁹ Although, Fillingham et al. (2019) show that it is also possible for the star formation epoch of Boo I to have ended prior to infall into the MW.

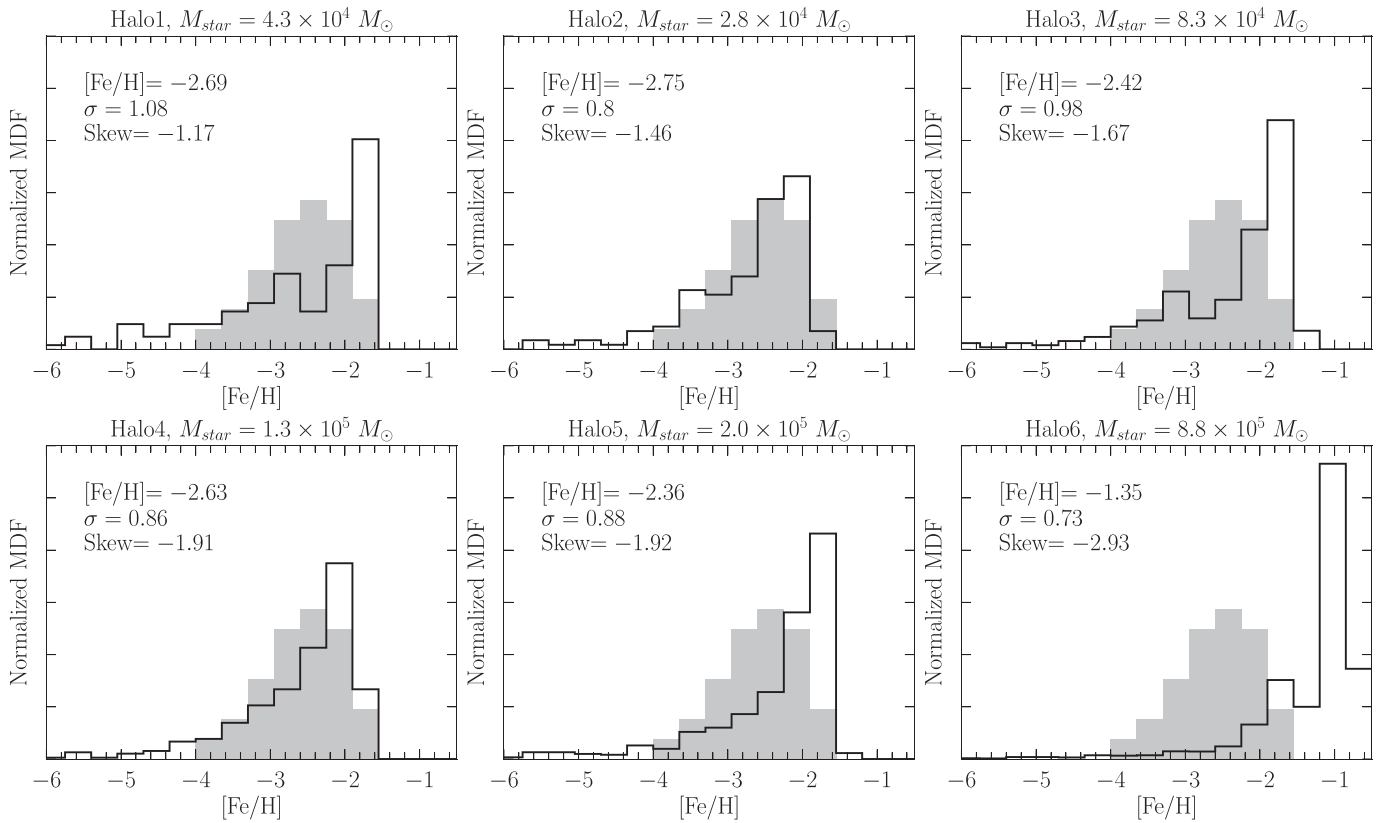


Figure 10. Comparison of the MDF that we derive for Eri II (gray shaded histogram; $M_{\text{star}} \sim 1 \times 10^5 M_{\odot}$, $[\text{Fe}/\text{H}] = -2.50$, $\sigma = 0.42$, skew = -0.21) with the six UFD MDFs simulated from Jeon et al. (2017). Following convention in previous histogram plots, bin sizes are 0.35 dex wide. The stellar mass of the corresponding halo at $z = 0$ are in the title of each panel. We also compute the mean metallicity, metallicity dispersion, and skew of the simulated MDFs. All of the simulated MDFs are skewed relative to Eri II, with long metal-poor tails.

5.4. Interpretation of UFD MDFs in Cosmological Simulations

While one-zone chemical evolution models have been pivotal in building intuition around the relationship between galaxy MDFs and the physics driving their evolution, detailed simulations show that a subset of dwarf galaxies are affected by a combination of reionization (e.g., Dawoodbhoj et al. 2018; Graus et al. 2019), local environment (e.g., Applebaum et al. 2021), and internal stellar feedback (Su et al. 2018; Smith et al. 2019). While some studies have produced certain observed features, such as the SFH of isolated dwarf galaxies (e.g., Fitts et al. 2017; Revaz & Jablonka 2018), and have begun to resolve bulk properties such as mean metallicity in UFDs (e.g., Wheeler et al. 2019), the lack of robust MDF observations of UFDs have motivated few studies to extensively simulate UFD MDFs as tracers of their formation processes. Jeon et al. (2017) is one of the few studies so far that predict MDFs of UFDs by following the evolution of six halos with present-day stellar masses from $10^4 M_{\odot}$ to almost $10^6 M_{\odot}$. We use their MDFs as a point of comparison.

Figure 10 presents the MDF of Eri II, compared to the MDFs of the six simulated UFDs from Jeon et al. (2017). Halos labeled Halo1, Halo2, and Halo3 are UFD analogs whose star formation was ultimately shut off after reionization, though the study finds that both SNe and reionization are necessary to quench these galaxies. We consider these halos to have an SFH that is most analogous to that of Eri II. The remaining massive halos simulated were able to form stars after reionization through gas accretion and mergers. Comparing the MDF of the first three halos to Eri II, Halo2 has the MDF that is most

similar to that of Eri II, although within the simulation there is still variation in MDFs between halos that experienced similar SFHs and quenching mechanisms.

Regardless of mass, all of the simulated MDFs display long, metal-poor ($[\text{Fe}/\text{H}] < -4.0$) tails. In the simulation, these stars represent Population II stars that were directly enriched by the death of Population III stars at $z > 11$ in mini halos that later merged to form the final UFD analogs. This interpretation of the origin of the metal-poor tail is in contrast with the results of our one-zone fit to the MDF of Eri II, which also predicts a long, metal-poor tail, but which attributes it through chemical enrichment taking place in a single system rather than in the aggregate of many. Additional theoretical work to refine the interpretation of various components of MDFs would be of great interest in understanding small-scale galaxy formation. In any case, both comparison to one-zone models and cosmological simulations point to additional theoretical basis for expecting to find EMP stars in Eri II, and possibly in other UFDs as well. CaHK imaging studies with larger FoVs and increasing depths could uncover additional EMP candidates, but since these stars would have metallicities at the limit of discernment via CaHK, future discoveries would need to be confirmed via low-resolution spectroscopic studies on current facilities or observations on the next generation of ELTs (see, e.g., Sandford et al. 2020).

Finally, for each of the simulated MDFs, we also compute their mean metallicity, metallicity dispersion, and skew. The skew metrics confirm what we also verify visually: that all of the simulated MDFs from Jeon et al. (2017) are left-skewed

compared to that of Eri II, in part because our models do not reach below $[\text{Fe}/\text{H}] = -4.0$. As a result, the simulated MDFs tend to have a lower average metallicity than Eri II, and also larger metallicity dispersions.

Since there are stars in our sample that may be more metal-poor than $[\text{Fe}/\text{H}] = -4.0$ to within 2σ , improved metallicity measurements may populate the metal-poor tail of the MDF of Eri II. If Eri II also has a radial metallicity gradient decreasing outward, then measuring the metallicity of Eri II members out to larger radii may also bring the MDF of Eri II closer to predictions from this study.

More generally, since a viable theory of galaxy formation should be able to produce features of the UFD population, we suggest that future population-level comparisons between simulated and observed UFD MDFs could also account for MDF statistics. While the population of mean metallicity and metallicity dispersions would be useful baseline statistics to compare, we also suggest that higher-order moments such as skew and kurtosis would be important for capturing asymmetries in the shape of UFD MDFs, which are currently also represented in the one-zone models.

6. Conclusion

In this work, we combined HST WFC3/UVIS imaging in the narrowband F395N filter with broadband archival photometry to measure metallicities for 60 stars in Eri II, increasing the sample of member stars with known metallicities by a factor of nearly 4. We derive a mean metallicity of $[\text{Fe}/\text{H}] = -2.50^{+0.07}_{-0.07}$ and metallicity dispersion $\sigma_{[\text{Fe}/\text{H}]} = 0.42^{+0.06}_{-0.06}$, which is consistent with results from spectroscopic studies and with known trends about UFDs. We are able to independently confirm that Eri II is a UFD whose mean metallicity is consistent with properties of the general UFD population, and that it has a large internal metallicity dispersion. These results affirm the promise for HST CaHK narrowband photometry to faithfully recover the MDF properties of the fainter UFD counterparts of Eri II.

From an expanded sample of stellar metallicities, we fit one-zone chemical evolution models to the MDF of Eri II and find that it is best represented by a leaky box, similar to results from studies of LG isolated dwarf galaxies. We also present an updated orbit for Eri II, which suggests that it only recently fell into the MW. The composite of these results suggest that Eri II likely formed in an underdense region of the universe at high redshifts.

We also use our photometry to identify outliers in our derived MDF that may be promising targets for follow-up spectroscopy to (1) verify kinematic membership with Eri II, (2) refine the shape of the Eri II MDF at the most metal-poor end, and (3) conduct detailed chemical abundance analysis to infer sources of past enrichment events. Since the field of our narrowband imaging also includes the central cluster of Eri II, future work will also involve measuring the metallicity of the cluster as well.

Finally, having verified the efficacy of CaHK narrowband imaging for inferring the MDF of UFDs, our forthcoming publications will characterize the MDFs of the rest of the 18 UFD candidates observed by HST-GO-15901.

We thank Aaron Dotter for providing advance access to the MIST v2 models that include α enhancement. We thank Léo Girardi for adding F395N to the available set of simulated

filters in the TRILEGAL models for our work. We thank Clara Martínez-Vázquez for providing metallicity data from Martínez-Vázquez et al. (2021) for evaluation against our measurements. We thank Myoungwon Jeon for making the MDFs from Jeon et al. (2017) available for our analysis. We also thank Ani Chiti, Andrew Cole, Ting Li, Josh Simon, Evan Skillman, and Kim Venn for useful conversations about this work. S.W.F., D.R.W., M.B.K., A.P.J., and N.R.S. are thankful for the stimulating discussion at The Intersection of Age Measurements Across the Universe workshop hosted in Napa, California, in 2019 December. Finally, we thank the anonymous referee for comments that improved the quality of this manuscript.

S.W.F. acknowledges support from a Paul & Daisy Soros Fellowship, as well as from the NSFGRFP under grants DGE 1752814 and DGE 2146752. S.W.F. also acknowledges support from HST-GO-15901, HST-GO-16226 from the Space Telescope Science Institute, which is operated by AURA, Inc., under NASA contract NAS5-26555. D.R.W. acknowledges support from HST-GO-15476, HST-GO-15901, HST-GO-15902, HST-AR-16159, and HST-GO-16226 from the Space Telescope Science Institute, which is operated by AURA, Inc., under NASA contract NAS5-26555. E.S. acknowledges funding through VIDI grant “Pushing Galactic Archaeology to its limits” (with project number VI.Vidi.193.093) which is funded by the Dutch Research Council (NWO). N.F.M. gratefully acknowledges support from the French National Research Agency (ANR) funded project “Pristine” (ANR-18-CE31-0017) and from the European Research Council (ERC) under the European Unions Horizon 2020 research and innovation program (grant agreement No. 834148). M.B.K. acknowledges support from NSF CAREER award AST-1752913, NSF grant AST-1910346, NASA grant NNX17AG29G, and HST-AR-15006, HST-AR-15809, HST-GO-15658, HST-GO-15901, HST-GO-15902, HST-AR-16159, and HST-GO-16226 from the Space Telescope Science Institute, which is operated by AURA, Inc., under NASA contract NAS5-26555.

Software: DOLPHOT (Dolphin 2016, 2000), astropy (Astropy Collaboration et al. 2018), numpy (Oliphant 2006), matplotlib (Hunter 2007), emcee (Foreman-Mackey et al. 2013), corner (Foreman-Mackey 2016), scipy (Virtanen et al. 2020), dynesty (Speagle 2020).

Appendix A

Impact of Alpha Element Abundances on CaHK Photometry

Figure 11 compares the MIST models in CaHK color space for solar-scaled alpha abundances (left) to those for $[\alpha/\text{Fe}] = +0.4$ (right). At a given metallicity, the alpha-enhanced tracks are shifted down (redward) in CaHK space relative to the solar-scaled alpha tracks. For the more metal-poor models, the alpha-enhanced models also extend redder in F475W – F814W. Stars that fall outside the solar-scaled alpha grid are within the alpha-enhanced models.

If we recompute our MDF using the solar-scaled alpha models, we derive a mean metallicity of $[\text{Fe}/\text{H}] = -2.26 \pm 0.07$, and a metallicity dispersion of $\sigma_{[\text{Fe}/\text{H}]} = 0.44 \pm 0.06$. Thus, the MDF we derive would be more metal-rich, but the metallicity dispersion would remain unchanged. While alpha abundances changes our inferred stellar metallicities, these differences are not enough to account for the discrepancies between our measurements and

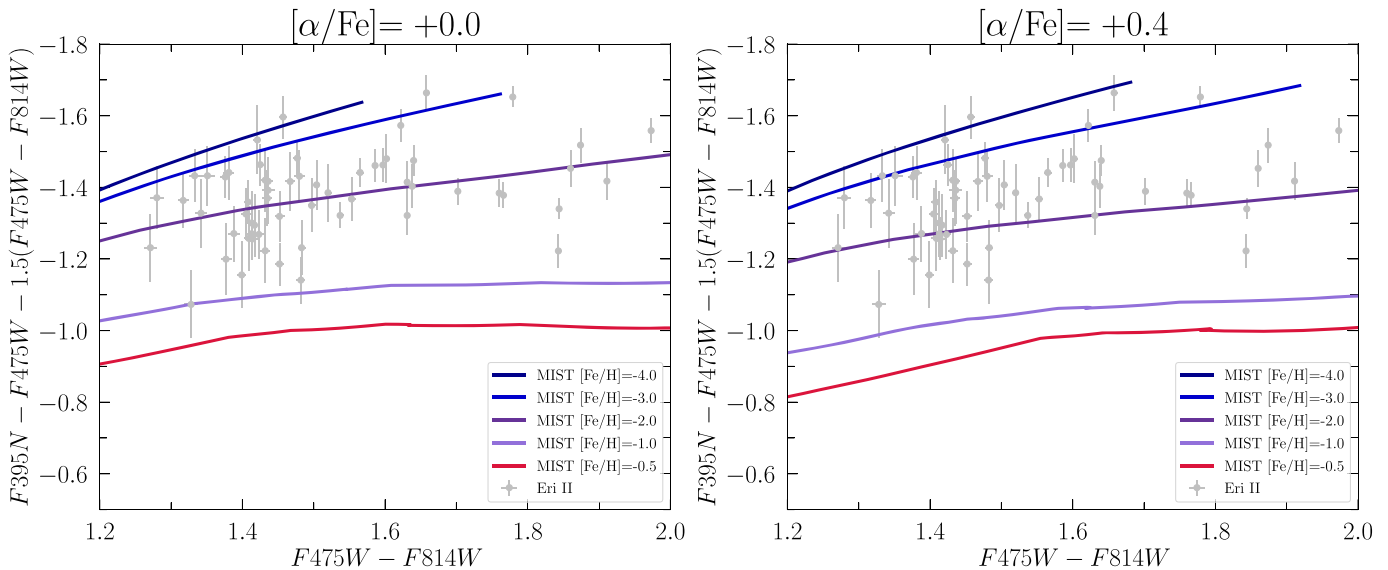


Figure 11. Comparing MIST isochrones in CaHK color space for isochrone models with $[\alpha/\text{Fe}] = 0.0$ (left panel) vs. $[\alpha/\text{Fe}] = +0.40$ (right panel). For an isochrone of a given metallicity, the α -enhanced model reaches redder extents in $F475W - F814W$, and is also redder in CaHK color index.

those of [Z20](#), since as [Figure 5](#) shows, the discrepancies in measurements are at least 1 dex or more.

Appendix B

Select Metallicity Posterior Distributions of Eri II Stars

In this section, we present select marginalized posterior distributions that result from our measurements of individual stellar metallicities.

[Figure 12](#) presents well-constrained marginalized posterior distributions. These distributions have a clear peak with clear

tails. Because CaHK is less effective at distinguishing between lower metallicities (e.g., [Figure 11](#)), the tails of these posterior distributions are often longer at the metal-poor end.

[Figure 13](#) shows the posterior distributions of stars that we identify as promising candidates for spectroscopic follow-up in [Section 4.5](#) and [Table 3](#).

[Figure 14](#) shows the posterior distributions of stars whose 2σ metal-poor tail extends beyond the lowest metallicity of our grid.

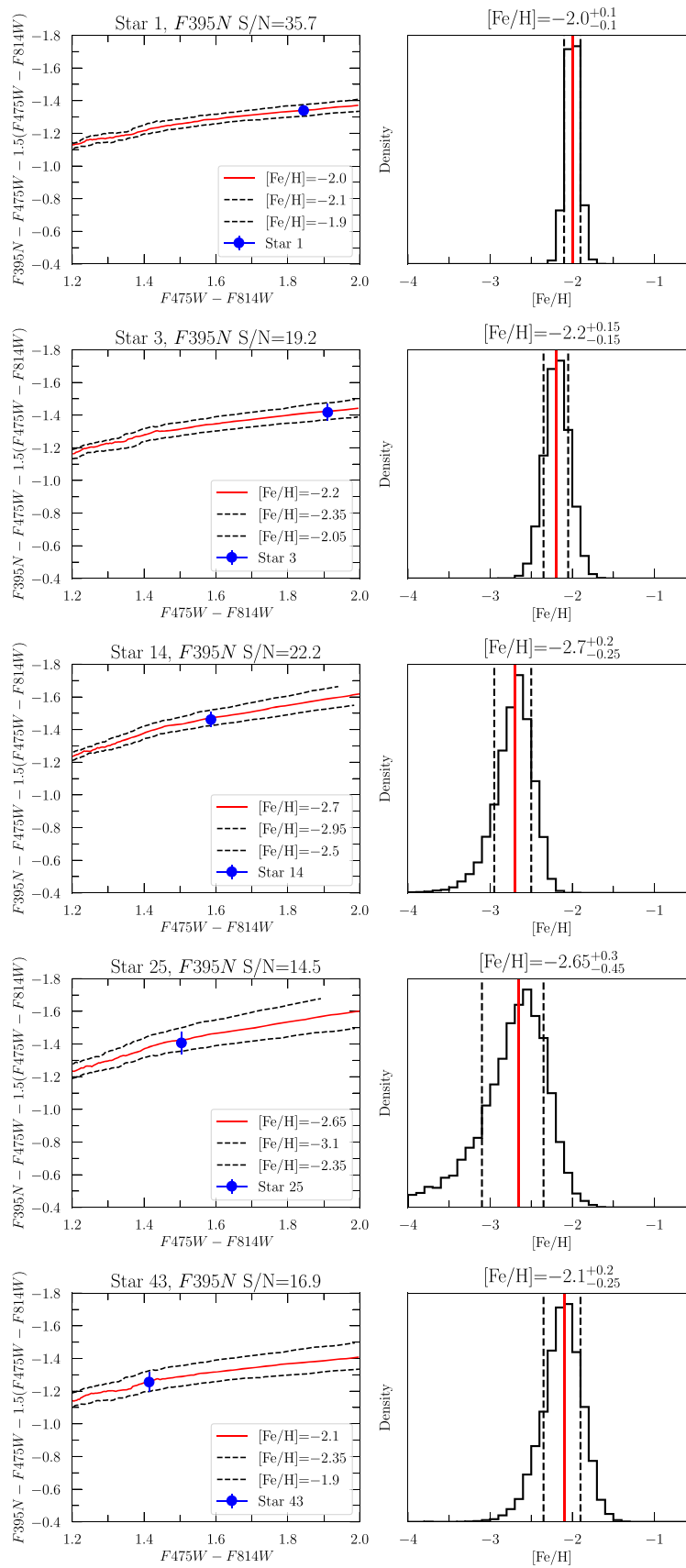


Figure 12. Well-constrained posterior distributions.

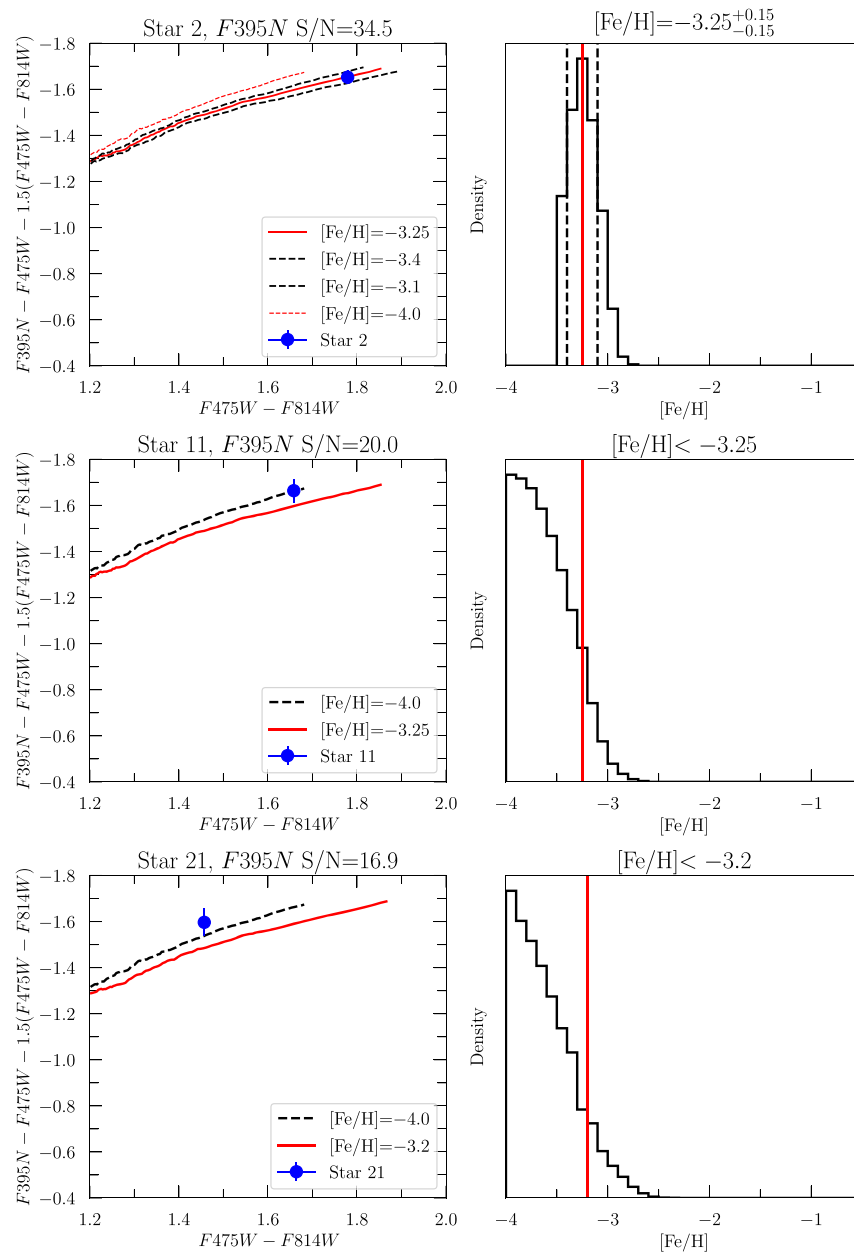


Figure 13. Posterior distributions of stars that we flag as spectroscopically accessible EMP candidates for follow-up studies, and which we discuss in Section 4.5.

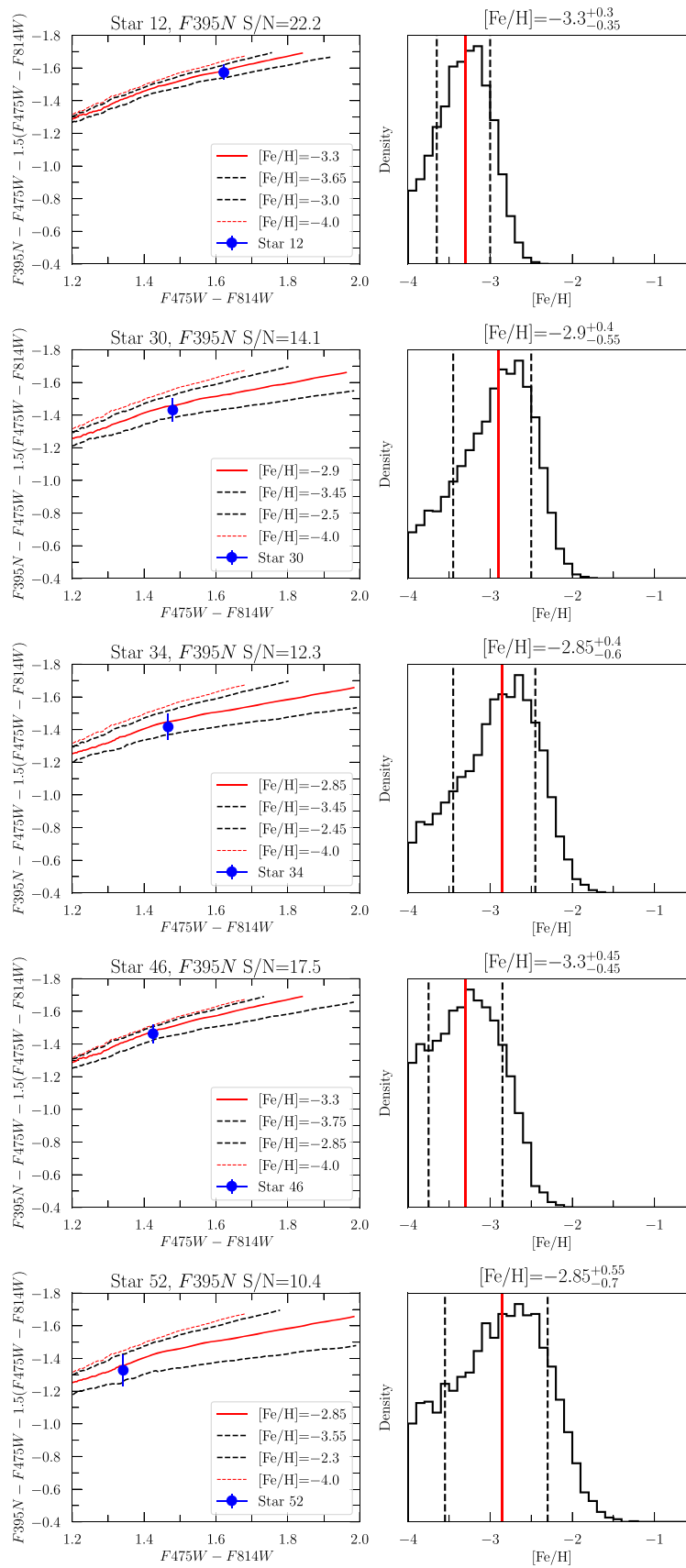


Figure 14. Posterior distributions of stars that are truncated at the 2σ level on the metal-poor end. The thin dotted red line is the most metal-poor ($[Fe/H] = -4.0$) model in our grid.

Appendix C Recovery of Synthetic MDF

In this section, we demonstrate the efficacy of the CaHK stellar metallicity inference methods applied in Section 3 by recovering a theoretical MDF from synthetic photometry. Figure 15 summarizes the results of this exercise.

First, we draw 60 stars from a Gaussian MDF with a mean and spread set by the values that we infer for Eri II in Section 4.3. We use the metallicities of those stars to draw model photometry from isochrones of corresponding metallicity, and ensure that the synthetic colors fall within the CaHK color space range set by our Eri II data. The top left panel of Figure 15 shows the location of the resulting model photometry in CaHK color space.

To arrive at the final catalog of synthetic photometries, we apply a bias and error to each model photometry point

following its corresponding error profile as determined by the ASTs from Section 2. We apply bias as an offset, and apply error as a random draw from a Gaussian corresponding to its AST uncertainty. We also adopt the error bar from our ASTs as the corresponding uncertainties for each synthetic photometric point. The top right panel of Figure 15 shows the final synthetic photometry in CaHK color space, with their corresponding uncertainties.

We then measure metallicities from the synthetic photometry following the procedures of Section 3. The bottom left panel of Figure 15 compares the input MDF to the recovered MDF, and the bottom right panel of Figure 15 compares the input metallicities to the recovered metallicities for individual stars. We verify that we can recover the input MDF and individual stellar metallicities following our method for inferring the MDF of Eri II.

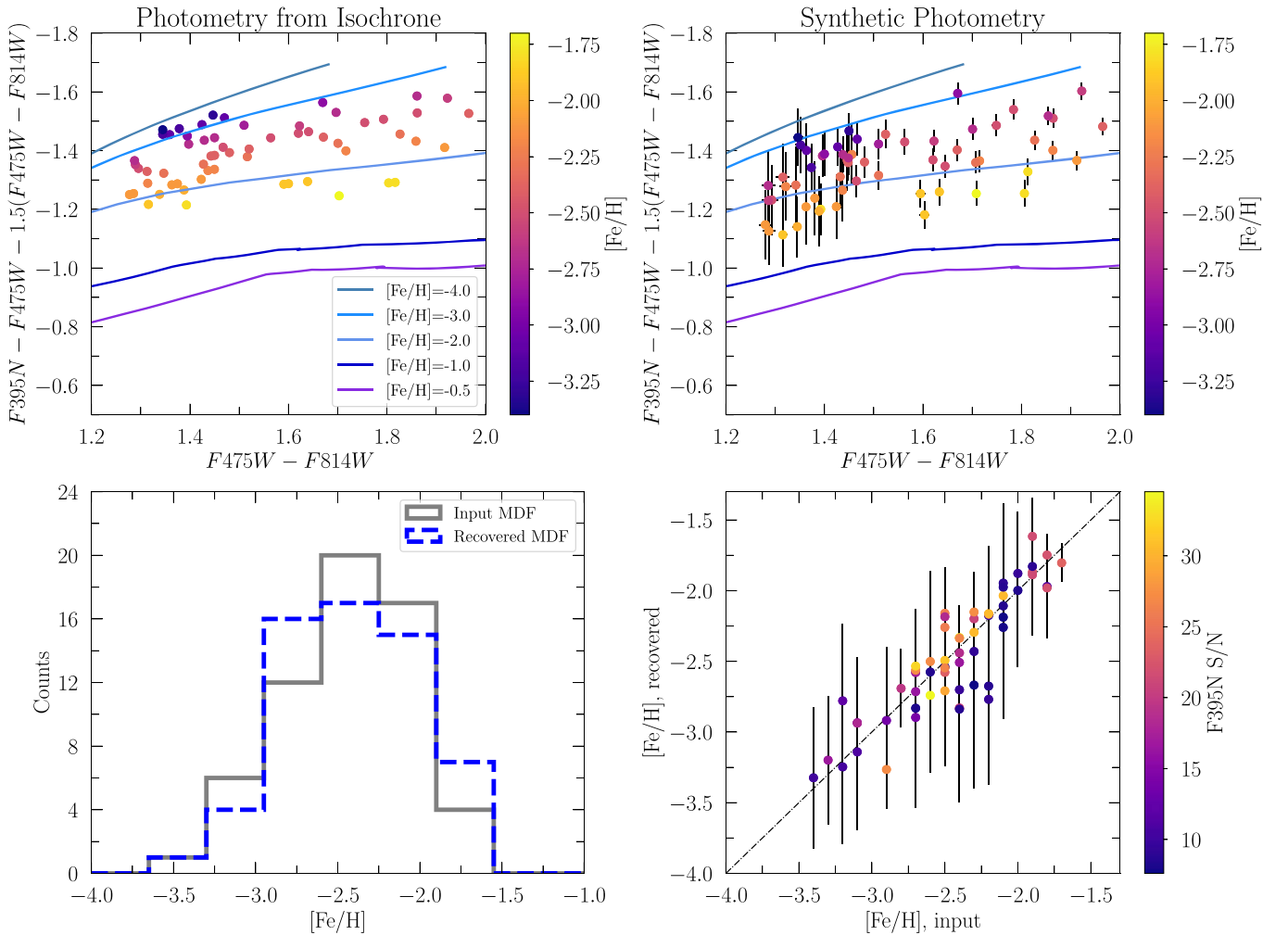


Figure 15. (Top left) the 60 model photometry points that we draw from isochrone models, with metallicity counts set by a Gaussian MDF with a mean and spread consistent with what we measure for Eri II. Points are color coded by their known metallicities. We also apply extinction to the tracks and the photometry in this plot, but it is negligible (on order of ~ 0.01 mag). (Top right) synthetic photometry after applying bias and uncertainty from the ASTs (described in Section 2 to the model photometry). As in the previous panel, points are color coded by their known metallicities. (Bottom left) comparing the input MDF to the MDF recovered after measuring individual stellar metallicities of the synthetic photometry, following the procedures in Section 3. (Bottom right) comparing the input metallicity to the recovered metallicity measurements for individual stars. Points are color coded by their synthetic F_{395N} S/N, as determined from the ASTs. The dashed-dotted line is a 1–1 relation.

Appendix D

Posterior Distributions of Analytic MDF Parameters

In this section, we present the posterior distributions of the Gaussian (Figure 16) fit to the MDF of Eri II, as well as those of the Leaky Box (Figure 17), Pre-Enriched (Figure 18), and Accretion (Figure 19) chemical evolution models. We tabulate fit parameters in Table 2.

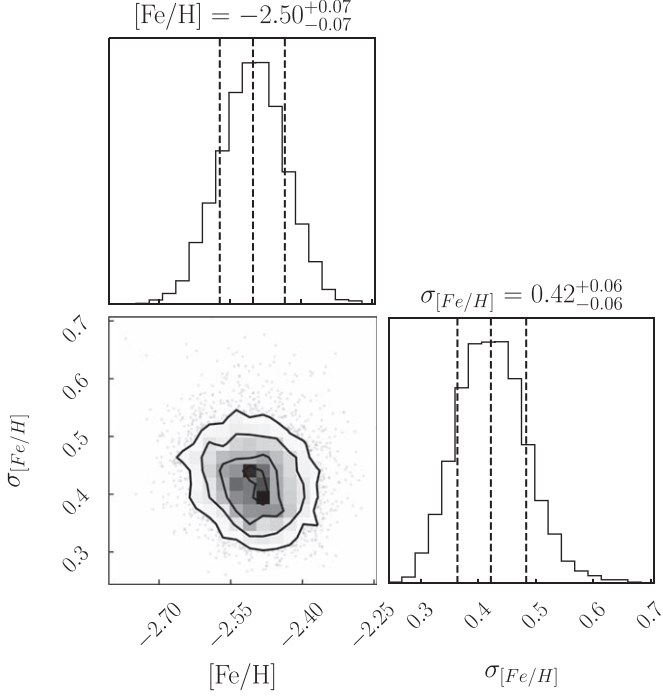


Figure 16. Joint distribution of the mean metallicity ($[Fe/H]$) and metallicity dispersion ($\sigma_{[Fe/H]}$) of Eri II. The dashed lines mark the 16th, 50th, and 84th percentiles of the 1D posterior distributions.

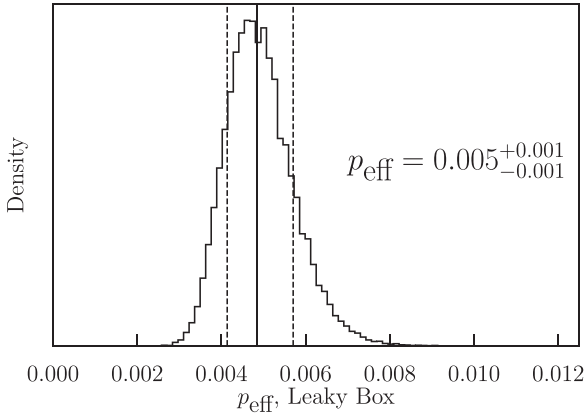


Figure 17. Posterior distribution of p_{eff} for the leaky box model.

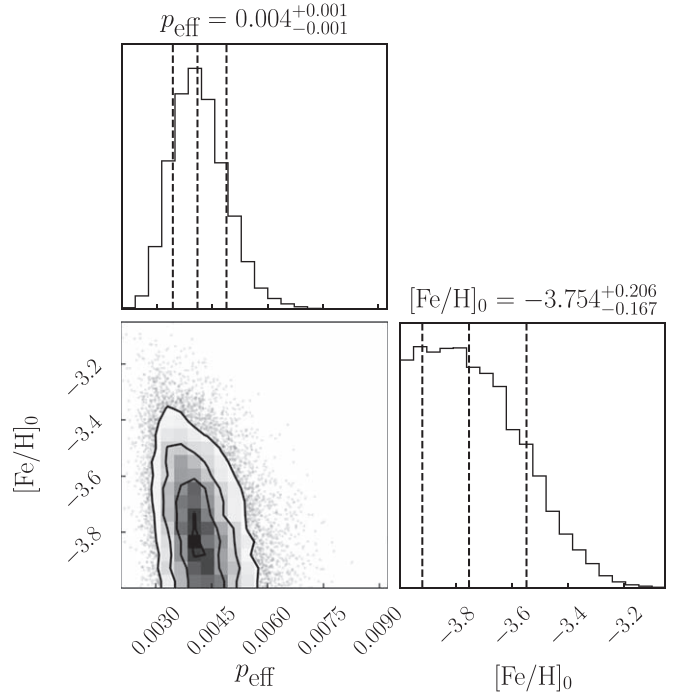


Figure 18. Posterior distribution corner plots of p_{eff} and $[Fe/H]_0$ for the pre-enriched gas model.

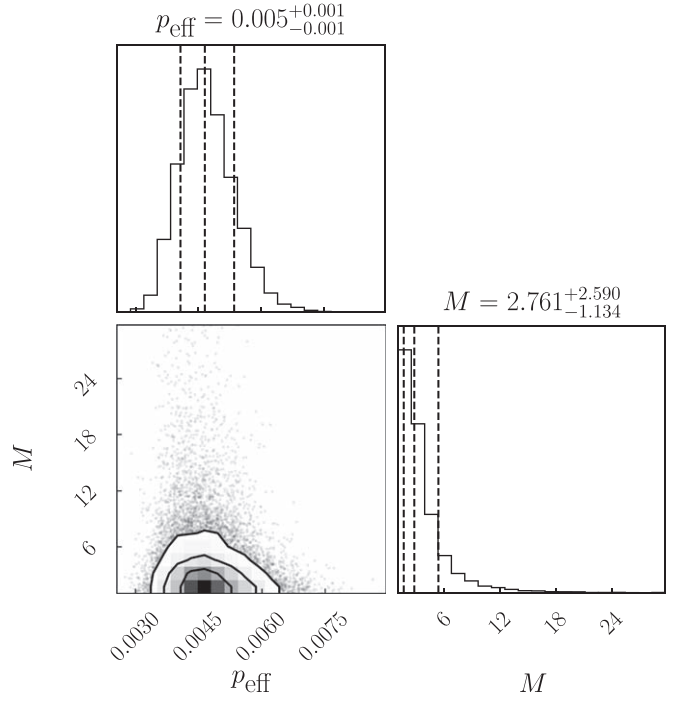


Figure 19. Posterior distribution corner plots of p_{eff} and M for the accretion model.

Appendix E

Table of Measurements

In this section, we present individual stellar metallicity measurements in Table 3.

Table 3
Metallicity Measurements for Eri II Stars

Star ID	R.A. (J2000) (deg)	Decl. (J2000) (deg)	F475W (mag)	F475W – F814W (mag)	CaHK (mag)	[Fe/H] _{perc} (dex)	[Fe/H] _{ulim} (dex)	[Fe/H] _{L17} (dex)	[Fe/H] _{Z20} (dex)
0	56.09995	-43.54543	21.243	1.973 ± 0.003	-1.558 ± 0.034	-2.55 ^{+0.10} _{-0.11}	...	-2.18 ± 0.14	...
1	56.11482	-43.52685	21.251	1.844 ± 0.002	-1.340 ± 0.028	-2.00 ^{+0.08} _{-0.08}
2 ^a	56.12385	-43.52998	21.288	1.779 ± 0.002	-1.653 ± 0.029	-3.24 ^{+0.16} _{-0.15}	...	-3.42 ± 0.15	...
3	56.11106	-43.52301	21.300	1.911 ± 0.003	-1.418 ± 0.052	-2.19 ^{+0.15} _{-0.15}	...	-1.85 ± 0.16	...
4	56.08661	-43.54101	21.392	1.874 ± 0.003	-1.518 ± 0.048	-2.52 ^{+0.15} _{-0.17}	...	-1.94 ± 0.20	...
5	56.08898	-43.50581	21.522	1.843 ± 0.003	-1.222 ± 0.047	-1.63 ^{+0.16} _{-0.15}	...	-1.92 ± 0.21	...
6	56.08422	-43.53636	21.578	1.860 ± 0.004	-1.453 ± 0.051	-2.33 ^{+0.15} _{-0.16}	-1.00 ± 0.10
7	56.06098	-43.52634	21.629	1.760 ± 0.003	-1.384 ± 0.038	-2.19 ^{+0.12} _{-0.12}	...	-2.54 ± 0.21	...
8	56.11060	-43.54553	21.642	1.766 ± 0.003	-1.378 ± 0.035	-2.17 ^{+0.11} _{-0.12}	...	-1.76 ± 0.22	...
9	56.07579	-43.51999	21.772	1.640 ± 0.003	-1.475 ± 0.043	-2.67 ^{+0.18} _{-0.21}	...	-2.63 ± 0.22	...
10	56.12467	-43.54148	21.781	1.702 ± 0.004	-1.389 ± 0.037	-2.25 ^{+0.12} _{-0.13}
11 ^a	56.09614	-43.52345	21.841	1.658 ± 0.004	-1.664 ± 0.050	-3.65 ^{+0.32} _{-0.24}	< -3.15	-2.82 ± 0.28	-2.14 ± 0.17
12 ^b	56.08598	-43.52225	21.964	1.622 ± 0.004	-1.573 ± 0.045	-3.31 ^{+0.32} _{-0.35}
13	56.07677	-43.55096	22.006	1.631 ± 0.003	-1.322 ± 0.053	-2.08 ^{+0.18} _{-0.19}
14	56.07042	-43.54281	22.010	1.586 ± 0.004	-1.461 ± 0.045	-2.69 ^{+0.20} _{-0.24}
15	56.06578	-43.54295	22.045	1.638 ± 0.003	-1.403 ± 0.061	-2.39 ^{+0.23} _{-0.25}
16	56.08129	-43.55030	22.062	1.631 ± 0.004	-1.415 ± 0.058	-2.44 ^{+0.22} _{-0.25}
17	56.08408	-43.50997	22.107	1.597 ± 0.004	-1.462 ± 0.047	-2.69 ^{+0.21} _{-0.25}
18	56.11464	-43.54801	22.206	1.537 ± 0.004	-1.321 ± 0.035	-2.18 ^{+0.13} _{-0.13}	...	-2.12 ± 0.22	...
19	56.07861	-43.54173	22.241	1.602 ± 0.004	-1.480 ± 0.068	-2.83 ^{+0.33} _{-0.47}
20	56.11415	-43.54755	22.336	1.565 ± 0.005	-1.441 ± 0.039	-2.63 ^{+0.17} _{-0.19}
21 ^a	56.07637	-43.53898	22.510	1.457 ± 0.005	-1.597 ± 0.059	-3.66 ^{+0.34} _{-0.24}	< -3.05
22 ^b	56.10017	-43.53943	22.666	1.477 ± 0.005	-1.482 ± 0.045	-3.18 ^{+0.35} _{-0.43}
23	56.09489	-43.54457	22.673	1.553 ± 0.005	-1.367 ± 0.061	-2.35 ^{+0.23} _{-0.26}
24	56.08373	-43.54938	22.764	1.520 ± 0.004	-1.385 ± 0.080	-2.54 ^{+0.33} _{-0.47}
25	56.07893	-43.52582	22.821	1.504 ± 0.004	-1.407 ± 0.069	-2.66 ^{+0.32} _{-0.45}
26	56.09459	-43.50749	22.833	1.482 ± 0.006	-1.141 ± 0.065	-1.59 ^{+0.26} _{-0.23}
27	56.09084	-43.50566	22.841	1.483 ± 0.005	-1.232 ± 0.076	-1.93 ^{+0.27} _{-0.28}
28	56.11173	-43.52713	22.852	1.413 ± 0.006	-1.301 ± 0.090	-2.40 ^{+0.40} _{-0.54}
29	56.10807	-43.53627	22.878	1.497 ± 0.005	-1.349 ± 0.074	-2.39 ^{+0.29} _{-0.38}
30 ^b	56.09227	-43.52335	22.923	1.480 ± 0.008	-1.431 ± 0.071	-2.88 ^{+0.39} _{-0.56}	-1.77 ± 0.16
31 ^b	56.12278	-43.53618	22.933	1.436 ± 0.006	-1.417 ± 0.055	-2.91 ^{+0.35} _{-0.48}
32	56.08301	-43.52886	22.954	1.421 ± 0.005	-1.532 ± 0.095	-3.41 ^{+0.50} _{-0.41}	< -2.60	...	-2.08 ± 0.21
33	56.09625	-43.55913	23.075	1.452 ± 0.006	-1.186 ± 0.059	-1.80 ^{+0.21} _{-0.20}
34 ^b	56.10423	-43.52568	23.093	1.467 ± 0.007	-1.416 ± 0.081	-2.87 ^{+0.43} _{-0.59}	-1.88 ± 0.25
35	56.06941	-43.52878	23.129	1.452 ± 0.007	-1.319 ± 0.070	-2.33 ^{+0.27} _{-0.35}
36	56.08063	-43.51725	23.140	1.405 ± 0.007	-1.326 ± 0.071	-2.51 ^{+0.33} _{-0.45}
37 ^b	56.06264	-43.54250	23.152	1.432 ± 0.008	-1.420 ± 0.087	-2.99 ^{+0.51} _{-0.62}
38	56.07344	-43.53673	23.161	1.409 ± 0.007	-1.258 ± 0.090	-2.18 ^{+0.36} _{-0.46}
39 ^b	56.07087	-43.53055	23.169	1.435 ± 0.007	-1.369 ± 0.077	-2.66 ^{+0.39} _{-0.55}
40	56.07188	-43.53692	23.175	1.423 ± 0.007	-1.269 ± 0.067	-2.16 ^{+0.26} _{-0.30}
41	56.05765	-43.52671	23.177	1.413 ± 0.008	-1.271 ± 0.063	-2.19 ^{+0.24} _{-0.29}
42	56.07524	-43.52644	23.178	1.408 ± 0.006	-1.359 ± 0.061	-2.65 ^{+0.32} _{-0.46}
43	56.11103	-43.55082	23.191	1.414 ± 0.007	-1.256 ± 0.059	-2.12 ^{+0.22} _{-0.25}
44	56.09105	-43.53941	23.197	1.417 ± 0.007	-1.294 ± 0.087	-2.33 ^{+0.35} _{-0.51}
45	56.10678	-43.54770	23.209	1.432 ± 0.007	-1.223 ± 0.090	-1.97 ^{+0.33} _{-0.40}
46 ^b	56.07859	-43.51662	23.211	1.425 ± 0.006	-1.463 ± 0.057	-3.28 ^{+0.43} _{-0.46}
47 ^b	56.11409	-43.54579	23.218	1.376 ± 0.007	-1.429 ± 0.057	-3.30 ^{+0.43} _{-0.45}
48 ^b	56.08152	-43.53250	23.285	1.436 ± 0.009	-1.392 ± 0.093	-2.84 ^{+0.50} _{-0.67}
49 ^b	56.08677	-43.52698	23.286	1.381 ± 0.008	-1.442 ± 0.074	-3.29 ^{+0.49} _{-0.47}	-2.15 ± 0.22
50 ^b	56.06698	-43.53438	23.366	1.317 ± 0.007	-1.363 ± 0.076	-3.15 ^{+0.53} _{-0.53}

Table 3
(Continued)










Star ID	R.A. (J2000) (deg)	Decl. (J2000) (deg)	F475W (mag)	F475W – F814W (mag)	CaHK (mag)	[Fe/H] _{perc} (dex)	[Fe/H] _{ulim} (dex)	[Fe/H], L17 (dex)	[Fe/H], Z20 (dex)
51	56.09814	–43.54478	23.395	1.399 ± 0.006	–1.155 ± 0.093	–1.76 ^{+0.36} _{–0.35}
52 ^b	56.12947	–43.53420	23.529	1.342 ± 0.008	–1.328 ± 0.096	–2.86 ^{+0.54} _{–0.68}
53	56.12470	–43.53207	23.534	1.388 ± 0.008	–1.271 ± 0.077	–2.30 ^{+0.33} _{–0.42}
54	56.06552	–43.53220	23.635	1.377 ± 0.007	–1.200 ± 0.099	–2.03 ^{+0.39} _{–0.50}
55	56.10222	–43.51683	23.655	1.351 ± 0.010	–1.433 ± 0.083	–3.32 ^{+0.52} _{–0.46}	<–2.49
56	56.07829	–43.51428	23.675	1.333 ± 0.007	–1.433 ± 0.073	–3.41 ^{+0.50} _{–0.40}	<–2.64
57 ^b	56.11031	–43.54366	23.875	1.271 ± 0.009	–1.232 ± 0.094	–2.59 ^{+0.55} _{–0.74}
58	56.11346	–43.54091	23.903	1.328 ± 0.009	–1.073 ± 0.094	–1.62 ^{+0.36} _{–0.37}
59	56.11659	–43.54202	23.987	1.280 ± 0.009	–1.371 ± 0.088	–3.28 ^{+0.60} _{–0.49}	<–2.34

Notes. The columns are as follows: (1) Internal Star ID; (2) and (3) R.A. and decl.; (4) F475W mag; (5) F475W – F814W color; (6) CaHK index defined in Section 2; (7) [Fe/H] measurement based off the 16th, 50th, and 84th percentiles of each star’s PDF; (8) upper limit on [Fe/H] where relevant; (9) metallicity measurement from L17 where available; (10) metallicity measurement from Z20 where available.

^a Stars that we identify in Section 4.5 as being spectroscopically accessible for chemical abundance studies and/or to verify their EMP nature. We discuss them in Section 4.5.

^b Stars whose posterior distributions display clear peaks, but which are truncated at the metal-poor end, as discussed in Section 4.1.

ORCID iDs

Sal Wanying Fu  <https://orcid.org/0000-0003-2990-0830>
Daniel R. Weisz  <https://orcid.org/0000-0002-6442-6030>
Nicolas Martin  <https://orcid.org/0000-0002-1349-202X>
Alexander P. Ji  <https://orcid.org/0000-0002-4863-8842>
Ekta Patel  <https://orcid.org/0000-0002-9820-1219>
Michael Boylan-Kolchin  <https://orcid.org/0000-0002-9604-343X>
Patrick Côté  <https://orcid.org/0000-0003-1184-8114>
Andrew E. Dolphin  <https://orcid.org/0000-0001-8416-4093>
Nathan R. Sandford  <https://orcid.org/0000-0002-7393-3595>

References

- Agertz, O., Pontzen, A., Read, J. I., et al. 2020, *MNRAS*, 491, 1656
Aguado, D. S., Youakim, K., González Hernández, J. I., et al. 2019, *MNRAS*, 490, 2241
Alzate, J. A., Lora, V., Bruzual, G., Lomeli-Núñez, L., & Sodi, B. C. 2021, *MNRAS*, 505, 2074
An, D., Beers, T. C., Johnson, J. A., et al. 2013, *ApJ*, 763, 65
Anthony-Twarog, B. J., Laird, J. B., Payne, D., & Twarog, B. A. 1991, *AJ*, 101, 1902
Applebaum, E., Brooks, A. M., Christensen, C. R., et al. 2021, *ApJ*, 906, 96
Arentsen, A., Starkenburg, E., Martin, N. F., et al. 2020, *MNRAS*, 491, L11
Astropy Collaboration, Price-Whelan, A. M., Sipőcz, B. M., et al. 2018, *AJ*, 156, 123
Battaglia, G., Taibi, S., Thomas, G. F., & Fritz, T. K. 2021, arXiv:2106.08819
Bechtol, K., Drlica-Wagner, A., Balbinot, E., et al. 2015, *ApJ*, 807, 50
Beers, T. C., Preston, G. W., & Shectman, S. A. 1985, *AJ*, 90, 2089
Belokurov, V., Zucker, D. B., Evans, N. W., et al. 2007, *ApJ*, 654, 897
Bland-Hawthorn, J., Sutherland, R., & Webster, D. 2015, *ApJ*, 807, 154
Bovill, M. S., & Ricotti, M. 2009, *ApJ*, 693, 1859
Brown, T. M., Tumlinson, J., Geha, M., et al. 2014, *ApJ*, 796, 91
Buck, T., Macciò, A. V., Dutton, A. A., Obreja, A., & Frings, J. 2019, *MNRAS*, 483, 1314
Bullock, J. S., & Boylan-Kolchin, M. 2017, *ARA&A*, 55, 343
Cáceres, C., & Catelan, M. 2008, *ApJS*, 179, 242
Carney, B. W. 1979, *ApJ*, 233, 211
Carra, R., Pancino, E., Gallart, C., & del Pino, A. 2013, *MNRAS*, 434, 1681
Cenarro, A. J., Moles, M., Cristóbal-Hornillos, D., et al. 2019, *A&A*, 622, A176
Chiti, A., Frebel, A., Jerjen, H., Kim, D., & Norris, J. E. 2020, *ApJ*, 891, 8
Chiti, A., Frebel, A., Mardini, M. K., et al. 2021a, *ApJS*, 254, 31
Chiti, A., Frebel, A., Simon, J. D., et al. 2021b, *NatAs*, 5, 392
Choi, J., Dotter, A., Conroy, C., et al. 2016, *ApJ*, 823, 102
Clementini, G., Cignoni, M., Contreras Ramos, R., et al. 2012, *ApJ*, 756, 108
Crojević, D., Sand, D. J., Zaritsky, D., et al. 2016, *ApJL*, 824, L14
Dawoodbhoj, T., Shapiro, P. R., Ocvirk, P., et al. 2018, *MNRAS*, 480, 1740
de Boer, T. J. L., Tolstoy, E., Hill, V., et al. 2012, *A&A*, 539, A103
Dolphin, A. 2016, DOLPHOT: Stellar Photometry, Astrophysics Source Code Library, ascl:1608.013
Dolphin, A. E. 2000, *PASP*, 112, 1383
Dotter, A. 2016, *ApJS*, 222, 8
Eggen, N. R., Scarlata, C., Skillman, E., & Jaskot, A. 2021, *ApJ*, 912, 12
El-Badry, K., Wetzel, A., Geha, M., et al. 2016, *ApJ*, 820, 131
Fillingham, S. P., Cooper, M. C., Kelley, T., et al. 2019, arXiv:1906.04180
Fitts, A., Boylan-Kolchin, M., Elbert, O. D., et al. 2017, *MNRAS*, 471, 3547
Foreman-Mackey, D. 2016, *JOSS*, 1, 24
Foreman-Mackey, D., Hogg, D. W., Lang, D., & Goodman, J. 2013, *PASP*, 125, 306
Frebel, A., & Norris, J. E. 2015, *ARA&A*, 53, 631
Frebel, A., Simon, J. D., & Kirby, E. N. 2014, *ApJ*, 786, 74
Fritz, T. K., Battaglia, G., Pawłowski, M. S., et al. 2018, *A&A*, 619, A103
Gallart, C., Monelli, M., Mayer, L., et al. 2015, *ApJL*, 811, L18
Gallart, C., Monelli, M., Ruiz-Lara, T., et al. 2021, *ApJ*, 909, 192
Geisler, D., Claria, J. J., & Minniti, D. 1991, *AJ*, 102, 1836
Gelman, A., & Rubin, D. B. 1992, *StatSci*, 7, 457
Graus, A. S., Bullock, J. S., Kelley, T., et al. 2019, *MNRAS*, 488, 4585
Han, S.-I., Kim, H.-S., Yoon, S.-J., et al. 2020, *ApJS*, 247, 7
Harbeck, D., Grebel, E. K., Holtzman, J., et al. 2001, *AJ*, 122, 3092
Hartwick, F. D. A. 1976, *ApJ*, 209, 418
Held, E. V., Saviane, I., & Momany, Y. 1999, *A&A*, 345, 747
Helmi, A., Irwin, M. J., Tolstoy, E., et al. 2006, *ApJL*, 651, L121
Helmi, A., Ivezić, Ž., Prada, F., et al. 2003, *ApJ*, 586, 195
Ho, N., Geha, M., Tollerud, E. J., et al. 2015, *ApJ*, 798, 77
Huang, Y., Chen, B. Q., Yuan, H. B., et al. 2019, *ApJS*, 243, 7
Hunter, J. D. 2007, *CSE*, 9, 90
Husser, T. O., Wende-von Berg, S., Dreizler, S., et al. 2013, *A&A*, 553, A6
Irwin, M. J., Belokurov, V., Evans, N. W., et al. 2007, *ApJL*, 656, L13
Ivezić, Ž., Sesar, B., Jurić, M., et al. 2008, *ApJ*, 684, 287
Jenkins, S., Li, T. S., Pace, A. B., et al. 2017, *ApJ*, 820, 92
Jeon, M., Besla, G., & Bromm, V. 2017, *ApJ*, 848, 85
Jeon, M., Bromm, V., Besla, G., Yoon, J., & Choi, Y. 2021, *MNRAS*, 502, 1
Ji, A. P., Frebel, A., & Bromm, V. 2015, *MNRAS*, 454, 659
Ji, A. P., Frebel, A., Chiti, A., & Simon, J. D. 2016, *Natur*, 531, 610
Ji, A. P., Li, T. S., Simon, J. D., et al. 2020, *ApJ*, 889, 27
Ji, A. P., Koposov, S. E., Li, T. S., et al. 2021, *ApJ*, 921, 32
Kacharov, N., Battaglia, G., Rejkuba, M., et al. 2017, *MNRAS*, 466, 2006
Karaali, S., Bilir, S., & Tunçel, S. 2005, *PASA*, 22, 24
Karovicova, I., White, T. R., Nordlander, T., et al. 2020, *A&A*, 640, A25
Keller, S. C., Schmidt, B. P., Bessell, M. S., et al. 2007, *PASA*, 24, 1

- Kielty, C. L., Venn, K. A., Sestito, F., et al. 2021, *MNRAS*, **506**, 1438
- Kim, S. Y., & Peter, A. H. G. 2021, arXiv:2106.09050
- Kirby, E. N., Cohen, J. G., Guhathakurta, P., et al. 2013, *ApJ*, **779**, 102
- Kirby, E. N., Lanfranchi, G. A., Simon, J. D., Cohen, J. G., & Guhathakurta, P. 2011, *ApJ*, **727**, 78
- Kirby, E. N., Rizzi, L., Held, E. V., et al. 2017, *ApJ*, **834**, 9
- Kirby, E. N., Simon, J. D., & Cohen, J. G. 2015, *ApJ*, **810**, 56
- Koposov, S. E., Belokurov, V., Torrealba, G., & Evans, N. W. 2015, *ApJ*, **805**, 130
- Laevens, B. P. M., Martin, N. F., Bernard, E. J., et al. 2015, *ApJ*, **813**, 44
- Lai, D. K., Lee, Y. S., Bolte, M., et al. 2011, *ApJ*, **738**, 51
- Leaman, R. 2012, *AJ*, **144**, 183
- Lenz, D. D., Newberg, J., Rosner, R., Richards, G. T., & Stoughton, C. 1998, *ApJS*, **119**, 121
- Li, T. S., Simon, J. D., Drlica-Wagner, A., et al. 2017, *ApJ*, **838**, 8
- Li, T. S., Simon, J. D., Pace, A. B., et al. 2018, *ApJ*, **857**, 145
- Longeard, N., Jablonka, P., Arentsen, A., et al. 2021b, arXiv:2107.10849
- Longeard, N., Martin, N., Ibata, R. A., et al. 2021a, *MNRAS*, **503**, 2754
- Longeard, N., Martin, N., Starkenburg, E., et al. 2018, *MNRAS*, **480**, 2609
- Lynden-Bell, D. 1975, *VA*, **19**, 299
- Marconi, M., Coppola, G., Bono, G., et al. 2015, *ApJ*, **808**, 50
- Martin, N. F., Ibata, R. A., Collins, M. L. M., et al. 2016, *ApJ*, **818**, 40
- Martínez-Vázquez, C. E., Monelli, M., Cassisi, S., et al. 2021, *MNRAS*, **508**, 1064
- McClure, R. D., & van den Bergh, S. 1968, *AJ*, **73**, 313
- McConnachie, A. W., & Venn, K. A. 2020a, *RNAAS*, **4**, 229
- McConnachie, A. W., & Venn, K. A. 2020b, *AJ*, **160**, 124
- Mercado, F. J., Bullock, J. S., Boylan-Kolchin, M., et al. 2021, *MNRAS*, **501**, 5121
- Muñoz, R. R., Côté, P., Santana, F. A., et al. 2018, *ApJ*, **860**, 66
- Munshi, F., Brooks, A. M., Christensen, C., et al. 2019, *ApJ*, **874**, 40
- Mutlu-Pakdil, B., Sand, D. J., Crmojević, D., et al. 2021, *ApJ*, **918**, 88
- Nadler, E. O., Drlica-Wagner, A., Bechtol, K., et al. 2021, *PhRvL*, **126**, 091101
- Nagasawa, D. Q., Marshall, J. L., Li, T. S., et al. 2018, *ApJ*, **852**, 99
- Oliphant, T. E. 2006, *A Guide to NumPy*, Vol. 1 (USA: Trelgol Publishing)
- Pagel, B. E. J. 1997, *Nucleosynthesis and Chemical Evolution of Galaxies* (Cambridge: Cambridge Univ. Press)
- Pagel, B. E. J., & Patchett, B. E. 1975, *MNRAS*, **172**, 13
- Patel, E., Kallivayalil, N., Garavito-Camargo, N., et al. 2020, *ApJ*, **893**, 121
- Revaz, Y., & Jablonka, P. 2018, *A&A*, **616**, A96
- Rodríguez Wimberly, M. K., Cooper, M. C., Fillingham, S. P., et al. 2019, *MNRAS*, **483**, 4031
- Romano, D., Bellazzini, M., Starkenburg, E., & Leaman, R. 2015, *MNRAS*, **446**, 4220
- Ross, T. L., Holtzman, J., Anthony-Twarog, B. J., et al. 2013, arXiv:1310.4553
- Ross, T. L., Holtzman, J., Saha, A., & Anthony-Twarog, B. J. 2015, *AJ*, **149**, 198
- Ryan-Weber, E. V., Begum, A., Oosterloo, T., et al. 2008, *MNRAS*, **384**, 535
- Sandford, N. R., Weisz, D. R., & Ting, Y.-S. 2020, *ApJS*, **249**, 24
- Saviane, I., Held, E. V., & Bertelli, G. 2000, *A&A*, **355**, 56
- Saviane, I., Held, E. V., Momany, Y., & Rizzi, L. 2001, *MmSAI*, **72**, 773
- Schlegel, D. J., Finkbeiner, D. P., & Davis, M. 1998, *ApJ*, **500**, 525
- Schmidt, M. 1963, *ApJ*, **137**, 758
- Schroyen, J., de Rijcke, S., Valcke, S., Cloet-Osselaer, A., & Dejonghe, H. 2011, *MNRAS*, **416**, 601
- Simon, J. D. 2018, *ApJ*, **863**, 89
- Simon, J. D. 2019, *ARA&A*, **57**, 375
- Simon, J. D., Brown, T. M., Drlica-Wagner, A., et al. 2021, *ApJ*, **908**, 18
- Simon, J. D., Li, T. S., Erkal, D., et al. 2020, *ApJ*, **892**, 137
- Smith, M. C., Sijacki, D., & Shen, S. 2019, *MNRAS*, **485**, 3317
- Speagle, J. S. 2020, *MNRAS*, **493**, 3132
- Starkenbug, E., Martin, N., Youakim, K., et al. 2017, *MNRAS*, **471**, 2587
- Strömgren, B. 1966, *ARA&A*, **4**, 433
- Su, K.-Y., Hopkins, P. F., Hayward, C. C., et al. 2018, *MNRAS*, **480**, 1666
- Tinsley, B. M. 1980, *FCPh*, **5**, 287
- Tolstoy, E., Hill, V., & Tosi, M. 2009, *ARA&A*, **47**, 371
- Tolstoy, E., Irwin, M. J., Helmi, A., et al. 2004, *ApJL*, **617**, L119
- Vanhollebeke, E., Groenewegen, M. A. T., & Girardi, L. 2009, *A&A*, **498**, 95
- Vargas, L. C., Geha, M., Kirby, E. N., & Simon, J. D. 2013, *ApJ*, **767**, 134
- Vargas, L. C., Geha, M. C., & Tollerud, E. J. 2014, *ApJ*, **790**, 73
- Venn, K. A., Kielty, C. L., Sestito, F., et al. 2020, *MNRAS*, **492**, 3241
- Virtanen, P., Gommers, R., Oliphant, T. E., et al. 2020, *NatMe*, **17**, 261
- Walker, M. G., Mateo, M., Olszewski, E. W., et al. 2006, *AJ*, **131**, 2114
- Walker, M. G., Mateo, M., Olszewski, E. W., et al. 2016, *ApJ*, **819**, 53
- Weisz, D. R., & Boylan-Kolchin, M. 2017, *MNRAS*, **469**, L83
- Weisz, D. R., Dolphin, A. E., Skillman, E. D., et al. 2014, *ApJ*, **789**, 147
- Weisz, D. R., Zucker, D. B., Dolphin, A. E., et al. 2012, *ApJ*, **748**, 88
- Wheeler, C., Hopkins, P. F., Pace, A. B., et al. 2019, *MNRAS*, **490**, 4447
- Whitten, D. D., Placco, V. M., Beers, T. C., et al. 2021, *ApJ*, **912**, 147
- Willman, B., Blanton, M. R., West, A. A., et al. 2005, *AJ*, **129**, 2692
- Willman, B., Geha, M., Strader, J., et al. 2011, *AJ*, **142**, 128
- Willman, B., & Strader, J. 2012, *AJ*, **144**, 76
- Youakim, K., Starkenburg, E., Aguado, D. S., et al. 2017, *MNRAS*, **472**, 2963
- Youakim, K., Starkenburg, E., Martin, N. F., et al. 2020, *MNRAS*, **492**, 4986
- Zinn, R. 1980, *ApJS*, **42**, 19
- Zoutendijk, S. L., Brinchmann, J., Boogaard, L. A., et al. 2020, *A&A*, **635**, A107